Nano Research

ISSN 1998-0124 CN 11-5974/O4
https://doi.org/10.1007/s12274-020-3126-9

Review Article

Two-dimensional materials for light emitting applications: Achievement, challenge and future perspectives

Yi Zhu[1,2,§], Xueqian Sun[1,§], Yilin Tang[1], Lan Fu[2], and Yuerui Lu[1] (✉)

[1] *Research School of Electrical, Energy and Materials Engineering, College of Engineering and Computer Science, the Australian National University, Canberra, ACT 2601, Australia*

[2] *Department of Electronic Materials Engineering, Research School of Physics and Engineering, the Australian National University, Canberra, ACT 2601, Australia*

[§] *Yi Zhu and Xueqian Sun contributed equally to this work.*

Received: 12 May 2020 / **Revised:** 28 August 2020 / **Accepted:** 22 September 2020

ABSTRACT

The two-dimensional (2D) materials have been widely developed recently in material characteristics with advanced optical and electrical properties, and they have been extensively studied as candidates for the next generation of optoelectronic devices. This review will mainly focus on the preparation methods and the light emitting applications of 2D transition metal dichalcogenides (TMDs), 2D black phosphorene (BP) and 2D perovskites. The review will first introduce the preparation methods for TMDs and BP. Due to the variations of band structure, exciton binding energies and light–matter interaction in TMDs and BP, the different light emitting devices (LEDs) designs based on TMDs and BP will be discussed and summarized. Then the review will turn the focus to 2D perovskites, starting with a description of the preparation methods for the different structural perovskites. In order to review and summarize the achievements of 2D perovskites-based LEDs, the high efficiency perovskites LEDs are discussed. Finally, the review will present challenges, opportunities, and outlook for the future development of 2D materials-based light emitting applications.

KEYWORDS

two-dimensional materials, light emitting devices, optoelectronic devices, perovskite, transition metal dichalcogenides (TMDs), perovskite light emitting device (LED)

1 Introduction

Two-dimensional (2D) materials are a class of materials originated from van der Waals solids. The tight ionic or covalent bonds are formed along 2D directions in between the in-plane atoms to form atomic layers, while the atomic layers are attached to each other by weak van der Waals force alone the out-of-plane direction [1, 2]. Nicolosi et al. have summarized different types of layered materials, which can be allocated into different families [3]. The atomically thin with hexagonal structured materials are the simplest, for example, graphene and hexagonal boron nitride (h-BN). There are some other layered materials such as transition metal dichalcogenides (TMDs), black phosphorene (BP), metal halides (for example PbI_2 and $MgBr_2$), layered metal oxides (such as MnO_2 and MoO_3), layered III-IVs materials (InSe and GaS), layered V-VIs materials (Bi_2Te_3 and Sb_2Se_3), and halide perovskites. In the past few years, research efforts have been devoted to TMDs and perovskites materials, many research progresses have been achieved in terms of studies of materials properties and device applications.

2D materials have attracted significant attention due to their fascinating optical and electrical properties [4–14]. 2D TMDs, unlike their precedent zero bandgap of graphene, are semiconductors with bandgap ranging from 1.57 to 2 eV [15], which are suitable for optoelectronic applications with visible and near infrared light regime. To be specific, 2D TMDs and phosphorene have demonstrated a series of interesting features such as tunable band structure [16–21], direct to indirect band transition [22–24], large exciton binding energies [25–28], strong light–matter interaction [29–32] and strong second harmonic generations [9, 33–36] that could trigger intensive studies of next generation optoelectronic devices such as light emitting diodes (LEDs) and photodetectors. The unique properties of 2D materials have been reviewed in several recent publications [19, 37, 38]. The light emitting properties of TMDs include photoluminescence (PL) and electroluminescence (EL) can be both modulated by many factors. For example, the PL can be tuned by substrate screening effect [39], temperature and even excitation power [40], while the EL can be adjusted by different geometry, current injection method, and electrostatic doping. Meanwhile, the PL and EL emission from those 2D materials provide a great platform for studying light–matter interaction including exciton dynamics, high order exciton behaviors, excitonic circuit and even exciton condensate [41–46]. Therefore, the light emitting applications in 2D materials system play a significant role in studying those ultra-thin semiconductors.

With promising research results on inorganic 2D TMDs and phosphorene, organic-inorganic halide perovskites are emerging

Address correspondence to yuerui.lu@anu.edu.au

as exciting materials for developing high-performance LEDs due to their unique structure and excellent optoelectronic properties [47]. However, in bulk perovskites, the stability, high leakage currents and non-radiative recombination losses are still the main issues of extending the LED application of those high yield materials. In order to solve those difficulties, two-dimensional perovskites have been brought into front line with variety of advantages that have not been observed in their three-dimensional (3D) counterparts because of 2D quantum confinement effect [48]. As a new member in 2D family, 2D perovskites have exhibited controllable synthesis, easy fabrication, flexible and high optical efficiency features, which enable them to achieve high efficiency LEDs devices [49–51].

For both traditional TMDs or phosphorene and new 2D perovskites, the common challenge for LEDs applications is to achieve high efficiency and unique light emitting features. To successfully emit light, two basic strategies have been employed. One is light emitting by forming a p-n junction within one material or different materials. The other is making use of semiconductor as an optical active layer, electrons and holes are then simultaneously injected into the semiconductor. The p-n junctions are commonly formed by chemical doping [52], electrostatic gating [53–55] and the use of different doping materials [56]. Both perovskites and TMDs are suitable for optical active layer, and they are ideal choice for fabricating high performance LEDs. In addition, TMDs based LEDs have been reported to observe single photon emission, which opens up new opportunities to quantum technologies [57].

In this review, we will first discuss the light emitting applications based on two-dimensional TMDs and phosphorene. Different well-designed LEDs device structures have been reviewed including different p-n junctions, optical active layer geometries, and driving methods. Their light emitting properties and optimization strategies will be emphasized. Subsequently, the single photon emissions from those TMDs and alternative current driven LEDs are discussed. Then we will review the recent progress on light emitting applications of 2D perovskites materials, starting with a discussion of their various synthesis methods and superb optoelectronic properties. After that, their light emitting devices and optoelectronic applications will be reviewed. Finally, the challenges, opportunities, and perspectives in the development of 2D materials light emitting applications will be stated.

2 Light emitting applications based on two-dimensional TMDs

The bandgap of the bulk TMDs is indirect, however, with the limitation of a single layer it becomes direct [22], fulfilling the most basic requirement for efficient light emission applications. The variety of TMDs with different bandgaps and working functions, on the one hand, allows for tuneable emissions over a wide range of wavelengths. On the other hand, it provides many opportunities for bandgap engineering of heterostructures [58]. The light emission properties based on TMDs are dominated by exciton species [59, 60]. The exciton in TMDs can be observed at room temperature owing to the quantum confinement and the strong Coulomb interaction. Excitons can be generated optically or electrically in TMDs forming different exciton species such as exciton, trion, biexciton and localized exciton, etc. Different exciton species can be tuned by chemical doping [61], electrostatic gating [62, 63] and even excitation power [64], which opens many routines to manipulate light emission properties. The LEDs are devices based on electroluminescence happened in semiconductor. Electroluminescence is a interesting physical phenomenon that converts electrical energy into optical energy, and usually the devices emit light originating from the electron and hole radiatively recombination. Therefore, the LEDs can be distinguished by driving methods such as direct current (DC) driven and alternative current (AC) driven. In DC driven LEDs, the devices can also be allocated into two groups according to whether the devices contain p-n junction or not. For AC driven LEDs, the device structure is similar to a capacity. In the following section, we will firstly discuss the preparation methods for TMDs and BP. Later we will discuss the TMDs and BP based LEDs with different structures and designs.

2.1 Preparation methods for 2D TMDs

Transition metal dichalcogenides with the chemical formula of MX_2, where M represents a transition metal (such as Mo and W) and X is a chalcogen (such as S, Se and Te). They are one class of the most studied inorganic 2D materials. Due to different stacking or metal-chalcogen coordination arrangement, different crystal types exist in TMDs. Taking MoS_2 as an example, it consists of four phases, which are 2H, 1T, 1T′ and 3R as shown in Fig. 1(a) [65]. The 2H phase is referred to

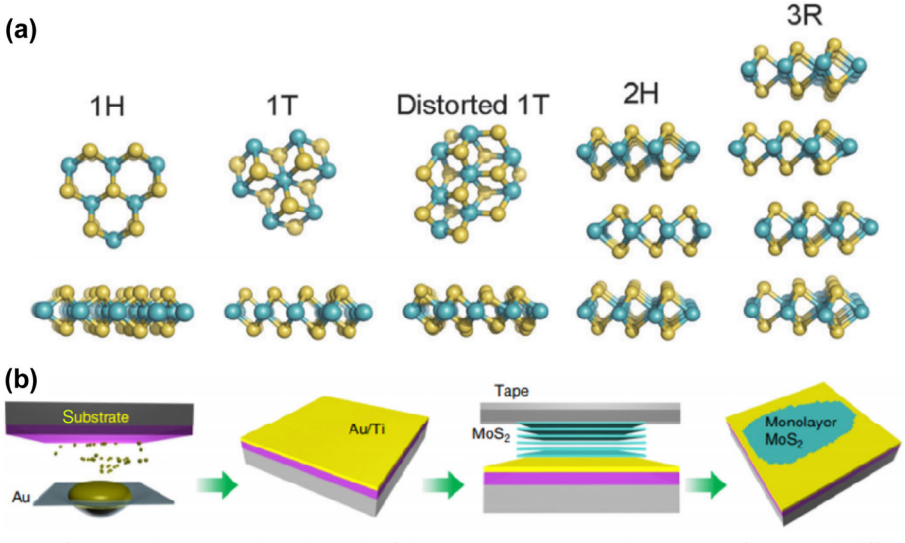

Figure 1 Crystal structures of MoS_2 and Au-assisted mechanical exfoliation process. (a) Crystal structures of MoS_2 with different phases. (b) Schematic of the Au-assisted mechanical exfoliation process. (a) is adapted with permission from Ref. [65], © The Royal Society of Chemistry 2015. (b) is adapted with permission from Ref. [77], © Huang, Y. et al. 2020.

crystal structure with trigonal prismatic coordination, while the octahedral coordination corresponds to 1T phase. The atomic stacking sequence is also different between 2H and 1T phase. For example, the S-Mo-S (ABA) in the hexagonal symmetry is conventionally referred to the 2H phase, and the 1T phase is S-Mo-S′ (ABA′) in the tetragonal symmetry. The 1T′ phase is considered as the disordered 1T phase with a similar octahedral coordination as the 1T phase. However, the 1T′ phase exhibits a superstructure in every layer, such as zigzag chain ($2a \times a$), trimerization ($\sqrt{3}a \times \sqrt{3}a$), and tetramerization ($2a \times 2a$) [65, 66]. The 3R phase consists of three atomic layers in one repeat unit under the rhombohedral symmetry with trigonal prismatic coordination. The 2H phase TMDs have been widely studied due to their superb optical properties. Therefore, this review will focus on 2H phase TMDs and their light emitting applications. The preparation methods for TMDs include exfoliation and chemical vapor deposition (CVD).

2.1.1 *Exfoliation*

The single to few layer TMDs can be prepared by breaking the weak van der Waals force between layers in their bulk materials. The exfoliation of bulk crystals includes mechanical exfoliation [29, 67–69], liquid phase exfoliation [70, 71], ion intercalation [72, 73], and plasma thinning technique [74, 75]. The mechanical exfoliation is mostly used in preparing ultra-high quality 2D layers as it is an all dry method that induces no other chemical contaminations. This method could quickly produce monolayer and few layers 2D materials but with low yield. In practical, some of 2D materials show difficulties in preparing thin layers by mechanical exfoliation. The ion intercalation method exhibits the advantage in preparing 2D materials that are hard to be obtained by mechanical exfoliation [76]. The plasma thinning technique is also known as the top-down strategy that can be used to achieve 2D thin layers with designed layer numbers. However, the plasma induced defects will be considered when the properties of the material have been investigated. Recently, Yuan Huang et al. reported a universal mechanical exfoliation of large are 2D materials by using an Au-assisted mechanical exfoliation method as shown in Fig. 1(b). Forty types of single crystalline monolayers have been successfully isolated by this modified mechanical exfoliation method due to the enhanced adhesion between the substrates and the crystals [77]. The gold-assisted exfoliation method could serve as a universal route for preparing monolayers with large area and thus supports investigations of fundamental physical properties and future potential applications of 2D materials.

2.1.2 *Chemical vapor deposition*

Chemical vapor deposition is the bottom-up strategy, which is direct synthesis or growth TMDs from their molecules. The CVD method has been widely used to synthesize single to multiple layer TMDs with regular or special structures [78–80]. Although CVD method is one of the most common way to produce 2D layer TMDs, the solid precursors used in furnace make it difficult to control the vapor pressure and supersaturation. Therefore, it restricts uniform growth of large area TMDs [81]. Instead of using solid phase precursors, the gas phase precursors used in metal-organic chemical vapor deposition (MOCVD) system show the possibility to grow high quality single and multiple layers of MoS_2 and WS_2 with wafer-scale homogeneity as presented in Figs. 2(a) and 2(b) [82]. In 2018, Jiadong Zhou et al. reported a molten-salt-assisted CVD method that can be employed to prepare a wide variety of TMDs and 2D materials [83]. The molten salt could not only effectively drop the melting points of metal precursors to reduce the synthesis temperature, but could also react with the metal oxides to form metal oxychlorides, which could evaporate at an suitable temperature and promote the growth of TMDs (Fig. 2(c)) [83]. More importantly, they have built a library of atomic thin metal chalcogenides that can be synthesized by this CVD method, which covers 47 compounds in total, including 32 binary compounds (consists of the transition metals Ti, Zr, Hf, V, Nb, Ta, Mo, W, Re, Pt, Pd and Fe), 13 alloys (including 11 ternary, one quinary and one quaternary), and two heterostructure compounds.

2.2 Light emitting properties in TMDs

In semiconductors, when a valence electron gains sufficient energy, it will move to the conduction band leaving behind a hole in the valence band. This electron becomes a conductive electron, which is free to move within the crystal lattice. Meanwhile, this electron and the hole can be attracted to each other by the Coulomb force to form a bound state, which is called exciton. The exciton is an electrically neutral quasiparticle that may exist in semiconductor. It has been widely studied as a two-particle system in III-V semiconductor system [84, 85]. The exciton binding energy is the minimum energy required to separate electron and hole pairs. For a typical III-V semiconductor such as GaAs, the exciton binding energy is only few meV such that the exciton can only be observed at low temperature. Compared with III-V semiconductor system, the 2D nature of monolayer TMDs leads to a strong enhancement of Coulomb interaction, as shown in Figs. 3(a) and 3(b). The significant consequence of strong Coulomb interaction is the formation of tightly bound excitons [86]. The exciton binding energy for MoS_2 is predicted to be between 0.5 and 1 eV [87, 88], and the measured value is 240 meV [89]. The exciton binding energy is measured to be 0.71 eV for monolayer WS_2 [90], 0.37 eV for monolayer WSe_2 [25], 0.55 eV for monolayer $MoSe_2$ [91], and 0.58 eV for monolayer $MoTe_2$ [63], which are much larger than those in typical III-V semiconductors with only 3.71 meV for InP and 4.76 meV for GaAs [92]. These large exciton binding energies from 2D materials allow us to observe the exciton dynamic at room temperature. Furthermore, thanks to the strong Coulomb interaction and quantum confinement in TMDs, higher order of exciton quasiparticles can be observed in TMDs system, which provides a distinct platform to study the many-body effect of excitons. In particular, when an exciton bounds with another electron or hole, it becomes a trion. Differed from neutral excitons, trions are charged quasiparticles. Exciton and trion competition in monolayer TMDs can be tuned by electrostatic gating and chemical doping as shown in Figs. 3(c)–3(h) [61, 62]. If two neutral excitons bound together, this four particles system is biexciton. The binding energy of biexciton is measured to be ~ 20 meV in monolayer $MoSe_2$ system [93]. Recently, some research groups have even observed charged biexciton, a five particles system, in h-BN encapsulated monolayer WSe_2, offering direct route towards deterministic control in many-body quantum phenomena. As described above, 2D TMDs naturally become an idea material system to study exciton dynamic and many-body interactions. The distinct optical properties of 2D TMDs have triggered a series of optoelectronic device applications such as light emission diodes. In the following section, the light emitting applications based on TMDs will be reviewed in detail.

2.3 LEDs based on TMDs p-n junction

The p-n junction is a key building block in optoelectronic applications including photodetectors and LEDs. Due to the

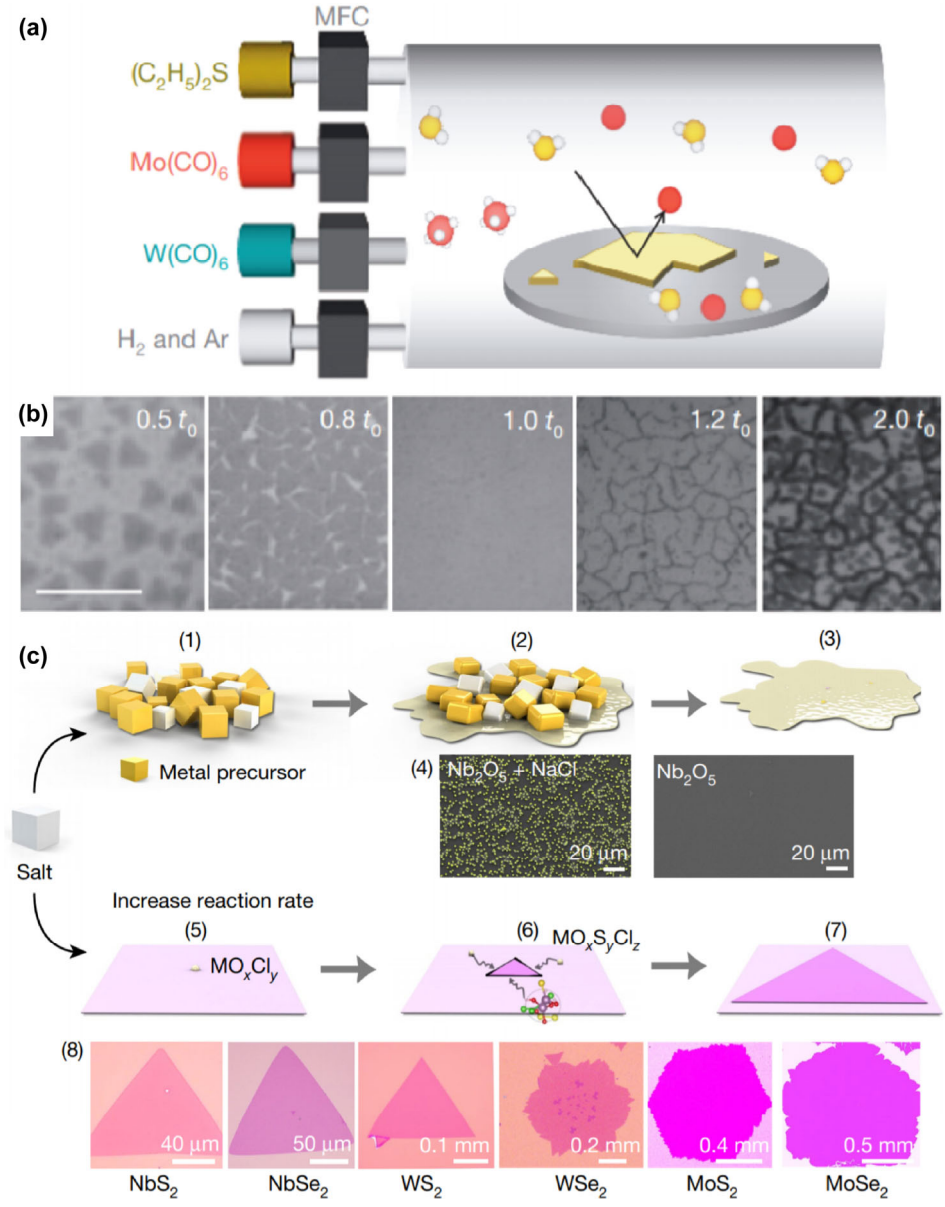

Figure 2 Chemical vapor deposition process for synthesizing 2D materials. (a) Schematic illustration of the synthesis of TMDs via MOCVD. (b) Optical images of MoS_2 grown by MOCVD with different growth times. The t_0 corresponds to growth time. Scale bar: 10 μm. (c) Schematics of the reactions. Metal oxychlorides are formed, and these promote the reactions. Chalcogens are not shown here. (1)–(3) The proposed process of the added salt decreasing the melting point of the precursors. (4) SEM images of the Nb nucleus with (left) and without (right) added salt. (5)–(7) The growth process of the 2D atomic layer, with intermediate products. (8) Different single-crystalline monolayers with large size of monolayer and a growth time of less than 3 min. (a) and (b) are adapted with permission from Ref. [82], © Macmillan Publishers Limited 2015. (c) is adapted with permission from Ref. [77], © Huang, Y. et al. 2020.

ultra-thin nature of TMDs, TMD materials are typically sensitive to the surrounding dielectric environment, allowing the possibility of electrostatic gating control of monolayer TMDs doping. Formation of a p-n junction by applying two split gates beneath the monolayer TMDs is a common technique. This concept has been employed to fabricate monolayer WSe_2 LED devices (Figs. 4(a) and 4(b)), demonstrating a total photon emission rate of ~ 16 million per second at the largest applied current of 35 nA, which corresponds to one photon per 10^4 injected electron–hole pairs [94]. Although the total estimated quantum efficiency is only 0.01%, the emission wavelength can be tuned between regimes of impurity-bound, charged and neutral excitons, as shown in Fig. 4(c). This splitting gate concept becomes popular for TMDs based LEDs. The electrical control enables a single device to have multiple functionalities. For example, ambipolar monolayer WSe_2 devices with splitting local gates have achieved both PN and NP configurations with diode ideal factors of n = 1.9 and a rectification factor of 10^5. The estimated electroluminescence quantum efficiency reached to ~ 1% [55]. To achieve light emitting in monolayer TMDs, the ambipolar field-effect transistor (FET) is another structure to form p-n junction within 2D materials [95]. By applying gate voltage, the TMDs can be effectively doped to neutral. Therefore, the TMDs based FET devices are able to operate in the ambipolar injection regime with holes and electrons injected simultaneously at the two opposite contacts in which light emission from the FET channel can be observed. This light emitting transistor based on monolayer WSe_2 devices have been achieved, as shown in Fig. 4(d) [96]. The circularly polarized electroluminescence can be emitted from p-i-n junctions that are electrostatically formed in transistor channels (Fig. 4(e)). This unique property can be explained qualitatively by the hole-electron overlap controlled by the in-plane electric field. The external quantum efficiency (EQE) varies from 0.002% to 0.06%

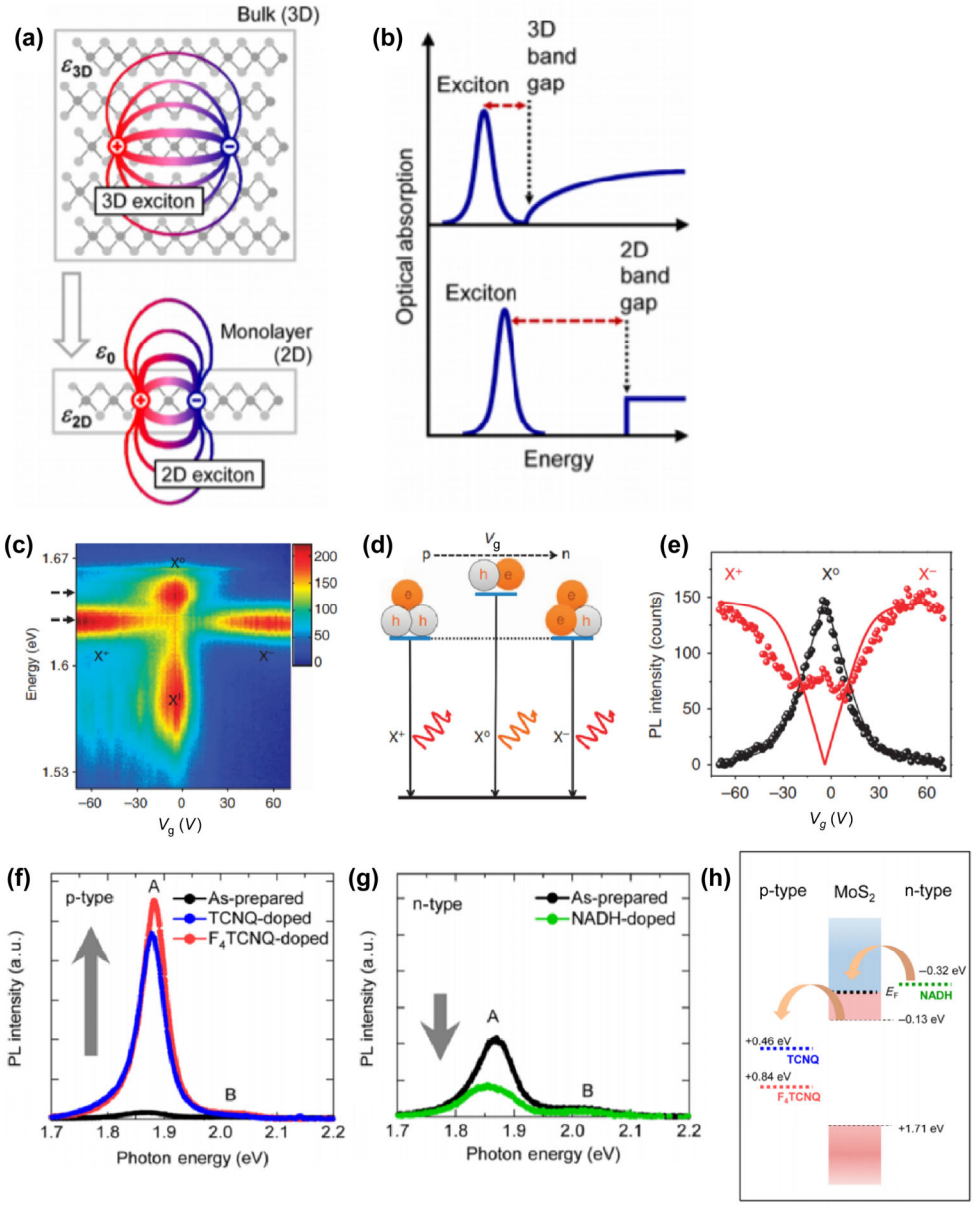

Figure 3 Exciton properties in 2D materials. (a) Schematic of the confinement of charge carriers and the reduced dielectric screening due to the absence of adjacent layers in 2D materials in comparison to bulk 3D materials. (b) Consequent increase of the band gap and exciton binding energy in semiconducting 2D materials. (c) $MoSe_2$ PL (colour scale in counts) is plotted as a function of back-gate voltage. Near zero doping, mostly neutral and impurity-trapped excitons are observed. With large electron (hole) doping, negatively (positively) charged excitons dominate the spectrum. (d) Illustration of the gate-dependent trion and exciton quasi-particles and transitions. (e) Trion and exciton peak intensity versus gate voltage at dashed arrows in (c). Solid lines are fits based on the mass action model. (f) PL spectra of 1L-MoS_2 before and after being doped with p-type molecules (TCNQ and F_4TCNQ). (g) PL spectra of 1L-MoS_2 before and after being doped with the n-type molecules (NADH). (h) Schematic of relative potentials (vs. SHE) of 1L-MoS_2 and n- and p-type dopants. (a) and (b) are adapted with permission from Ref. [86], © American Physical Society 2014. (c)–(e) are adapted with permission from Ref. [62], © Macmillan Publishers Limited 2013. (f)–(h) are adapted with permission from Ref. [61], © American Chemical Society 2013.

depending on samples (Fig. 4(f)). However, light emission from this lateral p-n junction devices is limited by the narrow one-dimensional junction interface, which results in low efficiency of LEDs. Therefore, vertically stacking TMDs to form p-n junctions are more favourable because of increased optical active area from a one-dimensional (1D) line to a 2D overlapping area. MoS_2 and WSe_2 vertical p-n junction LEDs are presented in Fig. 4(g), where the p-n junction area is covered over the entire MoS_2/WSe_2 overlapping area [97]. The electroluminescence from this device shows prominent band edge excitonic emission and strikingly enhanced hot-electron luminescence (Fig. 4(h)). However, the EL emission is localized at the overlapping area in close proximity to the electrodes instead of the entire overlapping area, as shown in Fig. 4(i). This phenomenon can be explained by the current injection in such p-n junction, which is limited by lateral contacts and lateral carrier transport owing to the depletion of the ultrathin TMDs. To realise a large and uniform area LEDs using this vertical p-n junction structure, it is imperative to achieve vertical current injection. Graphene as a uniform conductor can be employed into designing vertical p-n junction TMD LEDs. However, directly fabricating vertical contact on both top and bottom TMDs could lead to significant current leakage through ultrathin 2D materials. By using a quantum well structure, inserting a thin dielectric material between graphene and TMDs will dramatically minimize the current leakage and hence increase LEDs' efficiency. This structure is usually used in vertical stacking geometry and will be discussed in detail in the following sections.

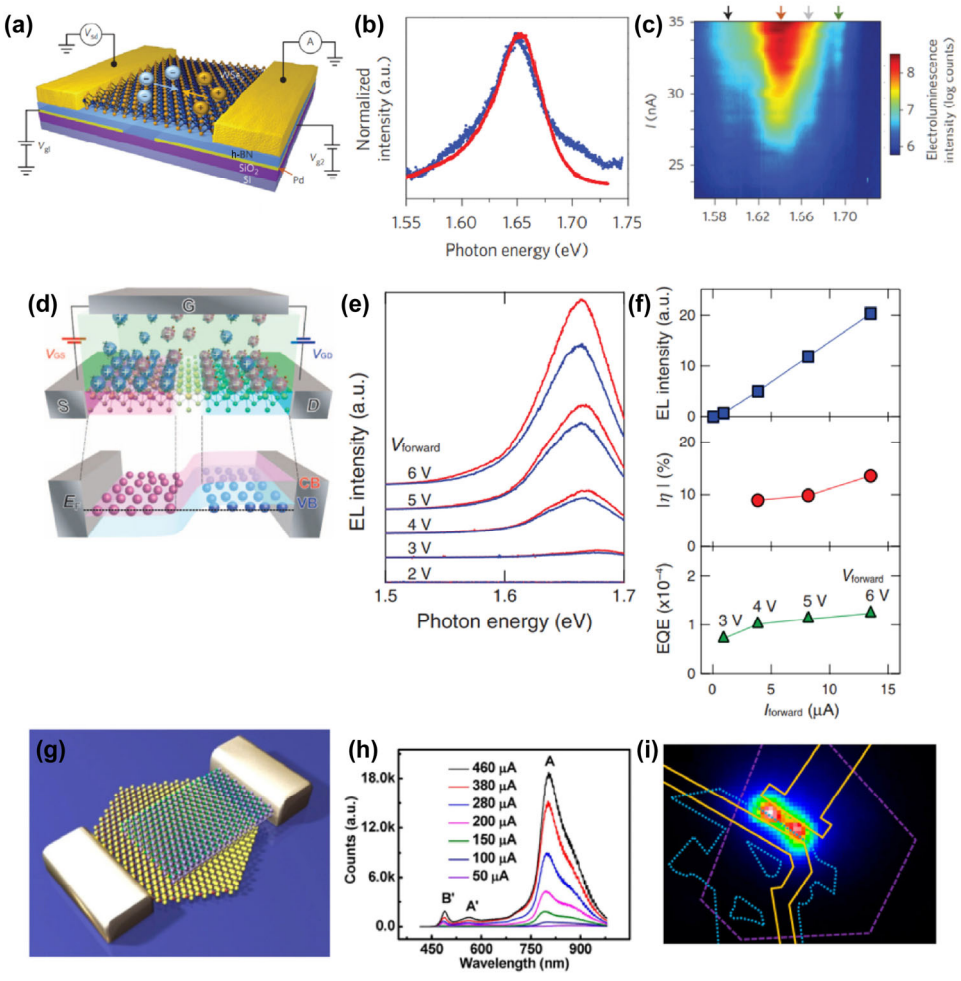

Figure 4 LEDs based on TMDs p-n junction. (a) Schematic plot of multiple monolayer WSe_2 p-n junction devices with palladium back gates (V_{g1} and V_{g2}) and source (S) and drain (D) contacts. The source–drain voltage (V_{sd}) is applied to one contact and the current (A) is read out of the other. During electroluminescence in the WSe_2, electrons (blue) and holes (yellow) move towards each other (arrows) and recombine. The back gates are separated from the WSe_2 by h-BN. The device sits on a layer of silicon dioxide on a silicon substrate. (b) Electroluminescence spectrum (blue) generated by a current of 5 nA closely resembles the photoluminescence spectrum (red) at 300 K. (c) Electroluminescence intensity plot as a function of bias current and photon energy. From left to right, the arrows indicate the impurity-bound exciton (X^I), the charged excitons (X^- then X^+) and the neutral exciton (X^0). (d) The upper panel is device structure of TMD electric-double-layer transistor (EDLT) under ambipolar charge accumulation. The bottom panel shows schematic band structure of EDLT induced p-i-n junction under equilibrium. (e) Voltage dependence of EL spectra of the device. (f) Upper: current dependence of total EL intensity extracted from (e). Middle: current dependence of EL polarization extracted from (e). Bottom: current dependence of external quantum efficiency extracted from (e). (g) Schematic illustration of the WSe_2/MoS_2 vertical heterojunction p-n diode. (h) The EL spectra of a ML-WSe_2/MoS_2 heterojunction at different injection current. (i) The false colour EL image of the heterojunction device under an injection current of 100 μA. The purple dashed line outlines the ML-WSe_2, the blue dotted line outlines the MoS_2 and the golden solid line outlines the gold electrodes. (a)–(c) are adapted with permission from Ref. [94], © Macmillan Publishers Limited 2014. (d)–(f) are adapted with permission from Ref. [96], © American Association for the Advancement of Science 2014. (g)–(i) are adapted with permission from Ref. [97], © American Chemical Society 2014.

2.4 LEDs based on TMDs vertical stacking

High efficiency and large area light emission of LEDs are desirable for many applications. Considering the drawbacks of p-n junction structures, people come up with a new design, named as vertically chip-based LEDs by stacking 2D materials layer by layer. In such a geometry, it usually consists of graphene, h-BN, and TMDs. For single optical active devices, two graphene layers, which served as the transparent uniform electrode contacts, are separated by an h-BN/MoS_2/h-BN sandwich quantum well, as shown in Fig. 5(a). The crucial part in this structure is the h-BN. The few layer h-BN serves as a tunnel barrier, which significantly reduces the leakage current when the device is operating with a current flowing from top to bottom layers. Especially, the thickness of the h-BN flake plays an important role in the LEDs operation. When the thickness of the h-BN flake is more than one atomic layer, the lifetime of the carriers could be sufficiently prolonged for the formation of excitons, which subsequently recombine to give efficient light emission (Fig. 5(b)). However, with the increase of the thickness of the h-BN, the current tunnel through the h-BN will dramatically decrease [98, 99], resulting in very weak LEDs emissions (Fig. 5(c)). The well-designed single h-BN/MoS_2/h-BN quantum well (QW) LEDs device exhibits ~ 1% quantum efficiency [100]. This efficiency can be further pushed to 8.4% by stacking four QWs, due to increased radiatively recombination [100]. This vertical stacking structure remarkably increased the light emitting quantum efficiency many orders of magnitude larger than the LEDs with p-n junction geometry. In addition, the emission spectrum can be finely tuned by combining different 2D semiconductors. The quantum efficiency of combinational devices reaches ~ 5% that is nearly comparable to those of current organic LEDs and state-of-the-art quantum dot LEDs. Based on those pioneering works, many following up works have been focussing on further optimisation of the

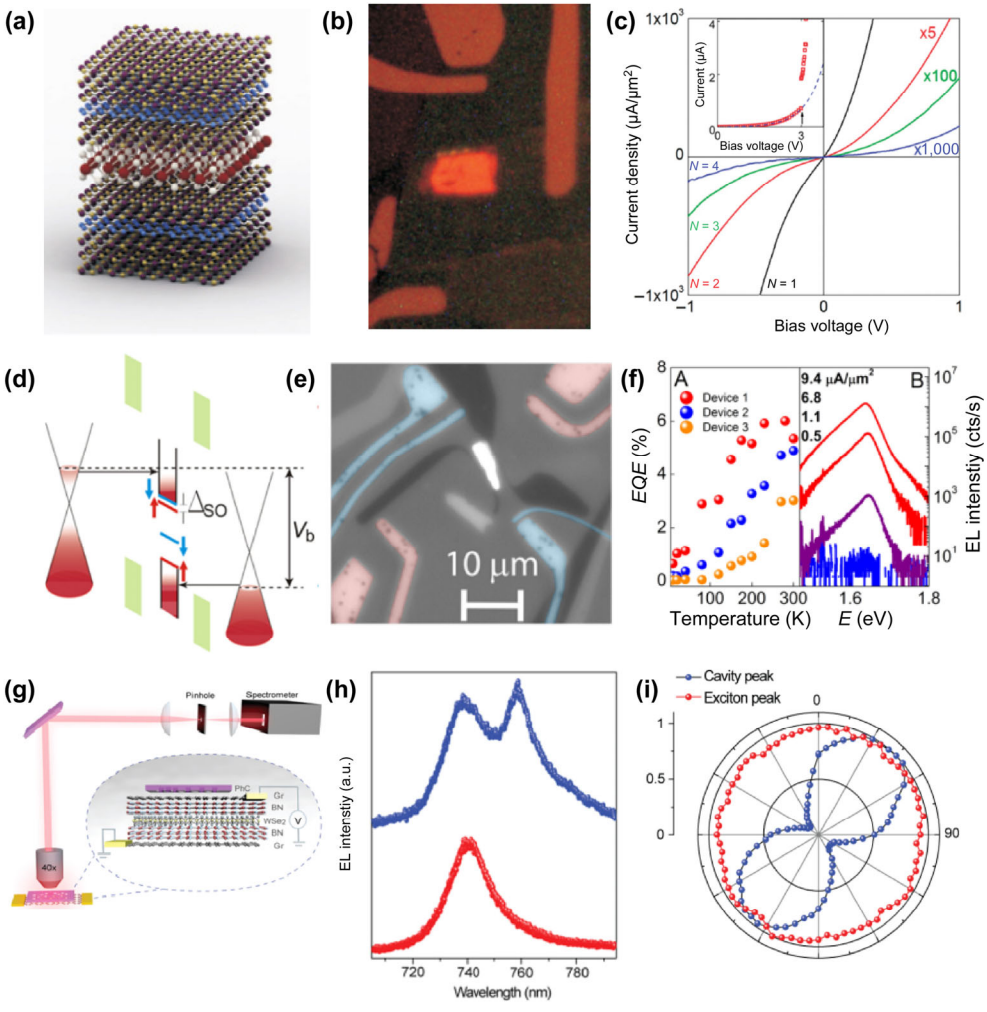

Figure 5 LEDs based on TMDs vertical stacking. (a) Schematic of the SQW heterostructure h-BN/Gr_B/2h-BN/WS_2/2h-BN/Gr_T/h-BN. (b) Optical image of EL from the same device. V_b = 2.5 V, T = 300 K. (c) Characteristic I–V curves for graphite/BN/graphite devices with different thicknesses of BN insulating layer: black curve, monolayer of BN; red, bilayer; green, triple layer; and blue, quadruple layer. Note the different scale for the four curves. Current was normalized by the realistic area of the tunnelling barrier, which ranged 2–10 μm^2 depending on the particular device. The inset shows a typical I–V curve where a breakdown in the BN is observed at +3 V, the thickness of the flake is 4 layers of BN (1.3 nm). The dotted line indicates the continuation of the exponential dependence. (d) Band alignment at high bias of a WSe_2 LEQW. (e) Magnification (50×) monochrome image of a WSe_2 LEQW device with an applied bias of V_b = 2 V and current of 2 μA taken in ambient conditions with weak backlight illumination (central white area corresponds to strong electroluminescence). Red false colour, Au contacts to bottom graphene, blue false colour, Au contacts to top graphene. (f) Left panel: temperature dependence of the quantum efficiency for three typical WSe_2 LED devices measured at bias voltages and injection currents of 2.8 V and j = 0.15 μA/μm^2 (Device 1), 2.8 V and j = 0.5 μA/μm^2 (Device 2), and 2.3 V and j = 8.8 μA/μm^2 (Device 3). Right panel: individual electroluminescence spectra plotted for four different injection current densities for Device 3. (g) Schematic of the EL measurement set-up and device architecture. (h)EL measured from (blue dots) and away (red dots) from the cavity area with V_b = 2 V. (i) Normalized cavity-enhanced peak intensity (blue dots) and exciton peak intensity (red dots) as a function of polarization detection angle. (a) and (b) are adapted with permission from Ref. [100], © Macmillan Publishers Limited 2015. (c) is adapted with permission from Ref. [98], © American Chemical Society 2012. (d)–(f) are adapted with permission from Ref. [101], © American Chemical Society 2015. (g)–(i) are adapted with permission from Ref. [102], © American Chemical Society 2017.

quantum efficiency by substrate modulation and integration with photonic crystal cavity. Room temperature high efficiency WSe_2 vertical stacking LEDs have been reported with refractive distributed Bragg refractor (DBR) substrates, as shown in Figs. 5(d) and 5(e). The function of DBR is to reduce the emission light scattering into SiO_2/Si substrates and enhance the light collection. Based on such DBRs, up to 30% of the emitted light can be collected, as opposed to just 2% collected from the Si/SiO_2 substrate. The EQE of WSe_2 devices increases with temperature (Fig. 5(f)), with EQE reaching 5% at room temperature [101], which is ~ 250 times more than the best performance of MoS_2 quantum wells in ambient conditions so far [100]. In Figs. 5(g) and 5(h), the integrated WSe_2 vertical stacking LEDs with integrated photonic crystal cavity have been reported. The EL emission efficiency has been enhanced by more than 4 times comparing with LEDs on bare SiO_2/Si substrate [102]. Such an enhancement was attributed to the strong coupling between the photonic crystal mode and exciton EL in WSe_2, leading to an increased emission rate. Moreover, the emission at the cavity resonance is single mode and highly linear polarized (84%) alone the cavity mode, as shown in Fig. 5(i). The photonic crystal cavity has realized the electrically pumped single mode light source, which is an essential step towards on-chip optical information technologies clearly indicating the important advantage of the vertical stacking LEDs structure. However, one challenge for this structure, as mentioned earlier, is the proper selection and preparation of the thickness of h-BN. The traditional method of mechanical exfoliation for preparing h-BN turns out to be difficult in term of observing the few layer h-BN flakes under microscope. Similar optical refractive index between h-BN and SiO_2 makes h-BN with less than five-layer nearly invisible. Many methods

have been proposed to solve this problem, such as using thinner SiO_2 (~ 80 nm) and using 470 or 590 nm light source to increase contrast [103]. Despite the complicated fabrication process of vertical stacking LEDs, it is still a giant leap for high efficiency TMDs based LEDs. With the rapid progress in technology of chemical vapor deposition growth of wafer scale TMDs will allow scaling up of production of such fancy LEDs devices.

2.5 Infrared LEDs based on TMDs and phosphorus

Infrared light spectral range is the vital part of wavelength band for optical communication and thermal imaging. It has been immensely used for civilian and military applications. Light sources and photodetectors within this bandwidth present on-going challenge [104, 105]. Traditional approaches for infrared light sources and lasers are based on III-V semiconductors and they are off-chip or wafer-bonded. Alternatively, the on-chip light source shows advantages for integrating into electronic or photonic circuits. The emerging 2D TMDs offer a new path way for optical interconnection components that can be integrated with industry silicon-based devices [82, 106, 107]. Monolayer $MoTe_2$ is a special member in 2D TMDs family with an electrical bandgap of ~ 1.72 eV [63, 108], The exciton emission peak from monolayer $MoTe_2$ is located at ~ 1.1 eV, which makes it a promising candidate for near infrared optoelectronic applications. Graphene/h-BN/$MoTe_2$ vertical stacking LEDs are presented in Fig. 6(a), where the device structure has been simplified from double tunnel barriers to a single tunnel barrier [109]. The $MoTe_2$ LED shows a high quantum efficiency of 9.5% at 83 K, as shown in Figs. 6(b) and 6(c). Such high quantum efficiency is attributed to 1) the dry membrane transfer, ultra-clean interface of devices, the delicate device structure and photolithography-free electrodes pattern technique; 2) low absorption from substrate at the emission wavelength of $MoTe_2$. It further confirms that the surface and substrate engineering are crucial for those atomic thin TMDs especially for device applications. In Fig. 6(d), the bilayer $MoTe_2$ based lateral p-n junctions with an electrostatic splitting gate configuration is presented. Moreover, the device was integrated with a silicon photonic crystal waveguide to demonstrate the potential for on-chip integration of light source and

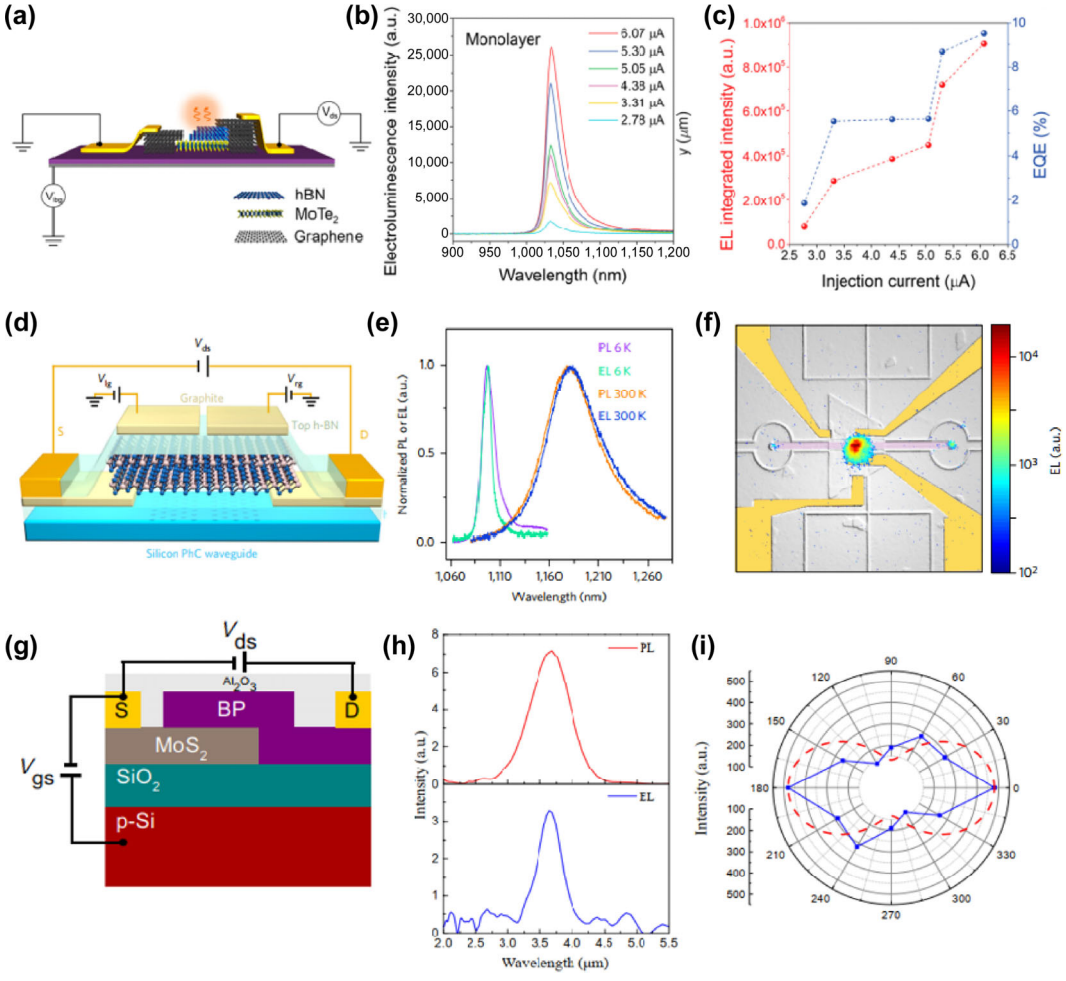

Figure 6 Infrared LEDs based on TMDs and phosphorus. (a) Schematic of the monolayer $MoTe_2$ LED and electrical connections for EL measurements. (b) EL spectra from monolayer $MoTe_2$ under different injection current and −20 V back gate voltage.(c) EL intensity (left) and EQE (right) of monolayer $MoTe_2$ as a function of the injection current. (d) Cross-sectional schematic of the encapsulated bilayer $MoTe_2$ p-n junction on top of a silicon PhC waveguide. The carrier concentration in $MoTe_2$ is controlled by the split graphite gates, the separation of the two gates is 400 nm, the dielectric layer is h-BN on top of the $MoTe_2$, and the thickness is 80 nm. The source (S) and drain (D) electrodes are thin graphite flakes connected to Cr/Au leads. (e) Spectrally resolved PL of the bilayer $MoTe_2$ flake and EL of the $MoTe_2$ p-n junction at room temperature and 6 K. The gate voltages of the p-n junction were set with opposite polarity $V_{lg} = -8$ V and $V_{rg} = 8$ V at a bias of $V_{ds} = 2$ V. (f) EL emission image at room temperature overlaid on top of a false-colour optical image of the device. Two extra emission spots from the grating couplers demonstrate coupling of the light source and silicon waveguide. (g) Schematic illustration of the cross-sectional view of the BP/MoS_2 heterojunction device. (h) Photoluminescence (red) and electroluminescence (blue) of the BP/MoS_2 diode. (i) Polarization resolved measurements of the EL intensity. (a)–(c) are adapted with permission from Ref. [109], © American Chemical Society 2018. (d)–(f) are adapted with permission from Ref. [110], © Macmillan Publishers Limited, part of Springer Nature 2017. (g)–(i) are adapted with permission from Ref. [113], © American Chemical Society 2020.

photodetector [110]. The strong EL emission intensity has been observed within p-n junction area where recombination happens. The EL emission wavelength is located at 1,090 nm at 6 K and 1,175 nm at room temperature respectively, as shown in Fig. 6(e). Figure 6(f) shows the EL intensity overlap with a false-color optical image of the structure at room temperature. The estimated waveguide coupling efficiency is 5%. This work demonstrates the possibility of integration of light emitting diodes and photodetectors with silicon photonic crystal waveguide, which enables point-to-point optical links and shows the potential of TMDs based near infrared light emitting system. Apart from $MoTe_2$, BP has emerged as another powerful 2D material with the bandgap ranging from ~ 0.3 to ~ 1.8 eV [16–18, 74, 111, 112]. The tuneable bandgap with different thicknesses covers the visible to mid-infrared spectral range, bridging the gap between graphene and TMDs. However, the stability issue greatly limits its optoelectronic application. Although the BP has been intensively studied since 2014, its device applications are mainly focused on photodetection properties. The BP based LEDs have been barely reported, due to the difficulties in device fabrications. To the best of our acknowledge, so far there is only one report on BP based LEDs, as presented in Fig. 6(g) [113]. The device consists of a 70 nm p-type BP layer on a 10 nm n-type MoS_2 layer to form a vertical p-n junction. The EL emission is at mid-infrared range of 3.68 μm (Fig. 6(h)), which agrees well with the reported measurements on thick BP flakes [114]. The emission pattern is polarized with a polarization ratio of ~ 3 for the AC to ZZ intensity, as shown in Fig. 6(i). The reported external quantum efficiency is about 0.03%, which is common for the p-n junction-based LEDs. Regardless of the stability issue with BP, this 2D material shows a very promising potential for applications in the infrared spectral range. For example, the five layered BP gives optical emission at 1,550 nm, which is located in optical communication bandwidth. The BP transistors show ambipolar field-effect with high hole mobility (in the order of 10 to 1,000 $cm^2/(V{\cdot}s)$) and current switching ratio of 100 to 10,000 [115–119]. With the further technology development in BP stabilization and large area material growth, continuing effort should be made to fabricate BP based high efficiency and fast speed optoelectronic devices.

2.6 Single photon emitter based on TMDs

Integrating high quality and high efficiency single photon sources into optoelectronic circuit is a key challenge to develop scalable quantum communication technologies [120]. Single photon emitters have been observed optically in monolayer WSe_2 due to the crystal structure imperfections that act as efficient carrier trapping center [121]. As the counterpart of optical pump, the electrical pumped single photon emissions are particularly suitable for developing quantum light generating devices. Inspired by the successful technique that used in TMDs based vertical stacking LEDs, WSe_2 and WS_2 atomically thin quantum LEDs have been reported [57]. The quantum LEDs employed a graphene/h-BN/TMD structure to realize carrier injections by changing the Femi level in graphene, which is shown in Figs. 7(a) and 7(b). When the device is in operation, the uniform light emitting is generated from the entire WSe_2 area. However, there is a hot spot observed in both monolayer and bilayer WSe_2 samples (Fig. 7(d)). Spectrum studies show that the emission behavior is different from free exciton recombination. In Fig. 7(c), the remarkably sharp peaks located at near infrared regime with linewidths ranging between 0.8 and 3 nm, suggesting that they belong to quantum emitters. To confirm they are single photon source, the intensity correlation function, $g^{(2)}(\tau)$, of EL emission from WSe_2 based quantum LEDs has been plotted as shown in Fig. 7(e). The value of the normalized $g^{(2)}(0)$, drops to 0.29 ± 0.08, well below the threshold value of 0.5, expected for a single-photon source [122]. Similarly, in WS_2 based quantum LEDs, quantum emitter was also observed with $g^{(2)}(0)$, dropping to 0.31 ± 0.05, which indicates that WS_2 supports stable QLED operation, generating single photons in the visible spectral range (Figs. 7(f) and 7(g)). It is noteworthy that single photon emission also can be achieved in WSe_2 LEDs with lateral p-i-n structures, as presented in Fig. 7(h) [123]. The devices show three single defects within narrow p-i-n junction area (Fig. 7(i)). Those defect emissions have a doublet with the characteristic exchange splitting and linearly polarized selection rules, which are consistent with previously reported properties of single photon emitters by optical measurements. Compared with the traditional bulk materials embedded solid-state single photon emitters, 2D materials are more suitable for on-chip integration with electronic circuits because of ultra-thin nature of 2D materials. However, the low yield of single photon emitter in 2D materials remains to be a challenge. How to create single photon emitters by controlled introducing of defects in TMDs is the next stepping-stone in developing TMD based single photon emitters.

2.7 AC driven LEDs based on TMDs

In above described LEDs structures, the electrical driven methods are all under direct current injection. It usually requires complicated structures and two electrode contacts. One challenge for them is that the Ohmic contacts in LEDs devices are essential to achieve high injection levels and minimize resistive losses [124]. Narrow p-n junctions and complicated structures limit the application for large area LEDs, for example the millimetre or even centimetre scale LEDs. Due to above limitations, research focus has been shifted from direct current injection to alternative current injection to seek breakthrough for large area emissions. The AC driven LEDs consist of a monolayer TMD sitting on a heavily doped Si substrate with a 50 nm thick SiO_2 and a single gold contact (Fig. 8(a)). The LEDs have been demonstrated for all four types of TMDs including WS_2, WSe_2, MoS_2, and $MoSe_2$, as presented in Fig. 8(b) [125]. Time resolved EL measurements indicate that the device only operates at the voltage transition with a transient EL signal, as presented in Figs. 8(c) and 8(d). With high frequency band bending of TMDs, electrons and holes are injected into the monolayer TMDs in separate cycles. The new injected carriers recombine with exit carriers that have opposite sign, then a bright light emission has been generated. Although the EL external quantum efficiency for WSe_2 LEDs, at current stage, is only 0.01%, the beauty of this AC driven LEDs is that the device does not require complex p-n junctions or heterostructures to achieve light emission, which provides the opportunity to scale up the devices to larger sizes. Based on this structure, centimetre scale monolayer AC driven LEDs have been achieved [126]. In Fig. 8(e)–8(g), the WS_2 based centimetre-scale (≈ 0.5 cm^2) visible (640 nm) spectrum has been demonstrated. It is worth noting that those AC driven LEDs are operating at room temperature, which demonstrates the possibility of operation under a more practical environment. However, the optimization of the device is still required to increase the device efficiency and the device lifetime. In addition, the AC driven LEDs have been proved to be a promising platform to observe the electrically driven high order correlated exciton states (Fig. 8(h)) [127]. By tailoring the parameters of the AC pulse, it is possible to generate either an electron or a

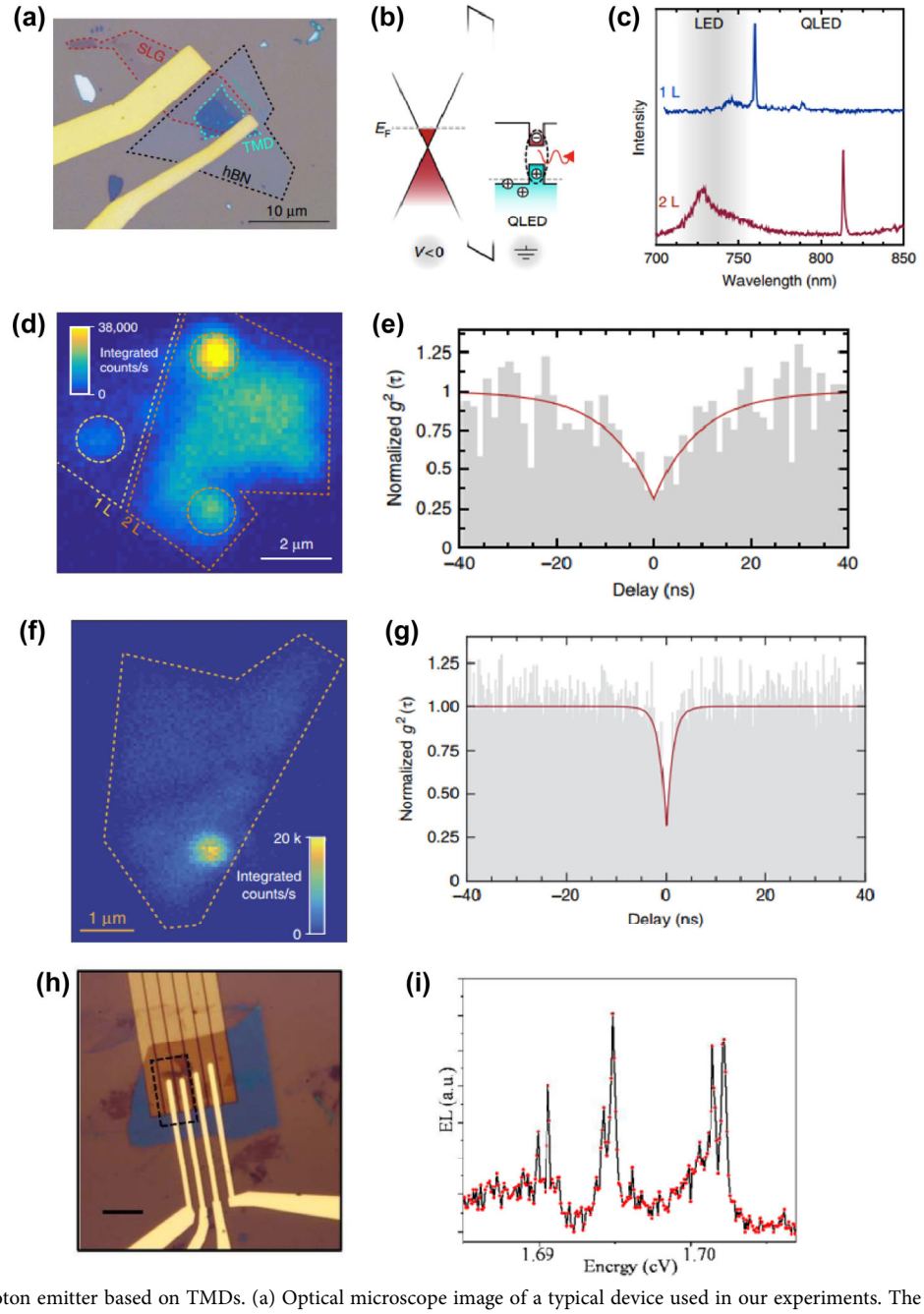

Figure 7 Single photon emitter based on TMDs. (a) Optical microscope image of a typical device used in our experiments. The dotted lines highlight the footprint of the single layer graphene (SLG), h-BN and the TMD layers individually. The Cr/Au electrodes contact the SLG and TMD layers to provide an electrical bias. (b) Heterostructure band diagram. Illustration shows the case for a finite negative bias applied to the SLG. (c) Typical EL emission spectra for quantum dots in the monolayer (top) and bilayer (bottom) WSe_2. The shaded area highlights the spectral window for LED emission due to bulk WSe_2 excitons, whereas QLED operation produces spectra at longer wavelengths. (d) A raster-scan map of integrated EL intensity from monolayer and bilayer WSe_2 areas of the QLED for an injection current of 3 mA (12.4 V). The dotted circles highlight the submicron localized emission in this device. (e) Intensity-correlation function, $g^{(2)}(\tau)$, for the same emitter displaying the anti-bunched nature of the EL signal, $g^{(2)}(0) = 0.29 \pm 0.08$, and a rise-time of 9.4 ± 2.8 ns. (f) A raster-scan map of integrated EL intensity from the monolayer WS_2 area of the device at 0.570 mA (1.97 V), where the highly localized QLED emission dominates over the unbound WS_2 exciton emission. (g) Intensity-correlation function, $g^{(2)}(\tau)$, for the same quantum dot displaying the anti-bunched nature of the EL signal, $g^{(2)}(0) = 0.31 \pm 0.05$, and a rise-time of 1.4 ± 0.15 ns. (h) Optical image of a lateral LED device. Scale bar is 15 μm. (i) EL spectrum for a lateral LED device showing emission from three single defects. (a)–(g) are adapted with permission from Ref. [57], © Macmillan Publishers Limited 2014. (h) and (i) are adapted with permission from Ref. [123], © American Chemical Society 2016.

hole rich environment in the 2D semiconductor, consequently favouring the diminished or enhanced EL from the different exciton species (Figs. 8(i) and 8(j)). Compared with DC driven LEDs, AC driven LEDs show the advantages of device simplicity and driving flexibility (frequency and amplitude). Unlike the DC driven LEDs, where electrons and holes are simultaneously injected into the material, the carriers injected into the AC driven LEDs is either electrons or holes, which provides more opportunity and freedom in studying carrier dynamics in such structures. However, improving the EL efficiency of AC driven LEDs is highly desirable. Optimising the system capacitance, engineering the radiative lifetime and biexciton recombination rate may be a promising approach for further improving the performance of TMD based AC driven LEDs.

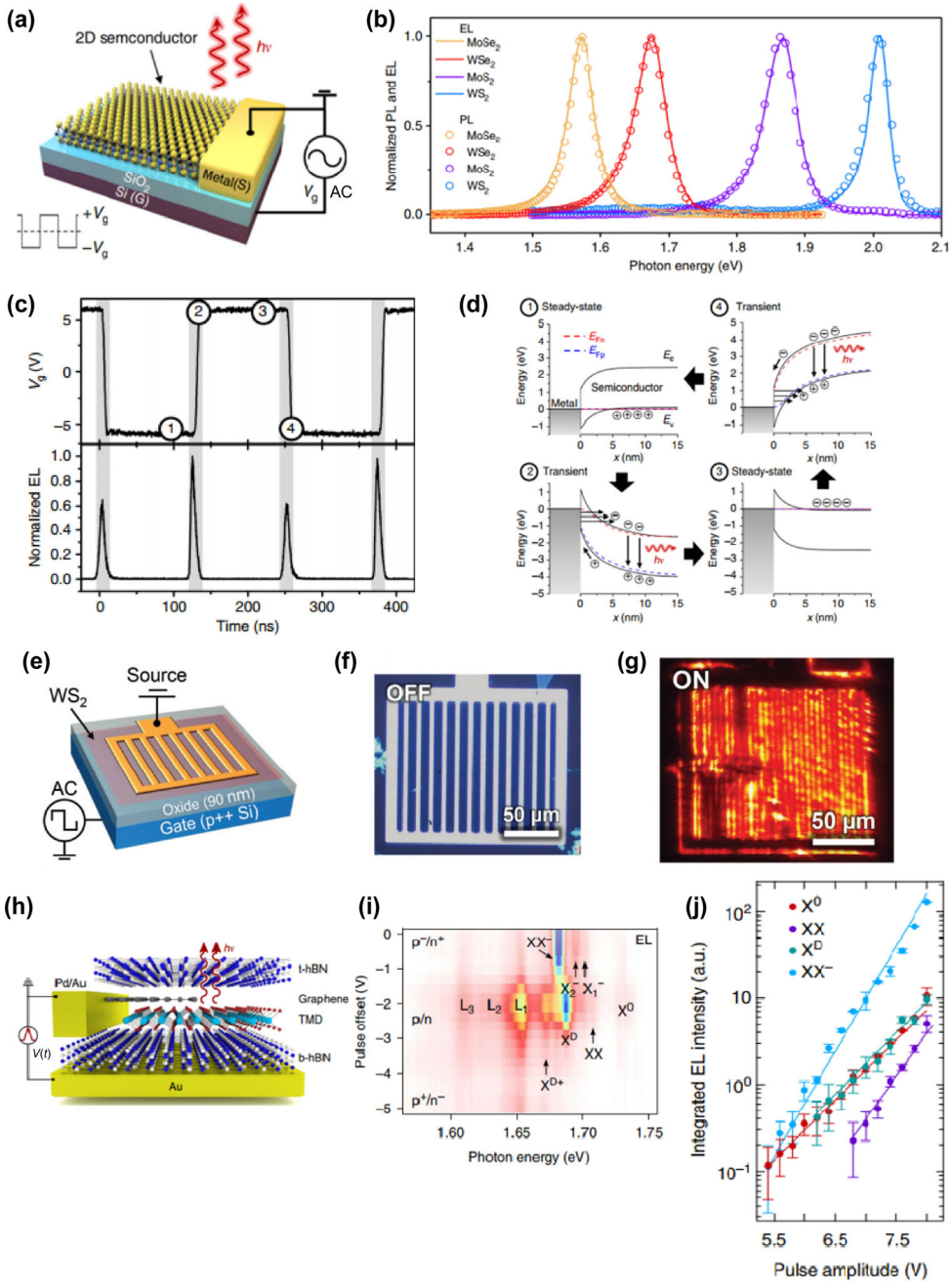

Figure 8 AC driven LEDs based on TMDs. (a) Schematic of the t-EL device. An AC voltage is applied between the gate and source electrodes and emission occurs near the source contact edge. (b) EL and PL spectra measured for $MoSe_2$, WSe_2, MoS_2, and WS_2 monolayer devices. (c) Time-resolved electroluminescence and the corresponding V_g, showing that EL occurs at the V_g transients (time points 2 and 4). (d) Band diagrams at different times during the operation cycle, corresponding to (c). E_{Fn} and E_{Fp} indicate the quasi-Fermi levels for electrons and holes, respectively. (e) Schematic of the t-EL device. (f) Optical microscope image of the fabricated t-EL device. (g) EL image of the device, showing emission is concentrated near the metal contacts. (h) Schematic drawing of the sample. The monolayer TMD and graphene are sandwiched between two multilayer h-BN flakes. (i) Emission spectra and tunability at T = 5 K. Pulsed EL from WSe_2. (j) Semi-logarithmic plot of the integrated EL intensity as a function of the pulse amplitude. The circles represent the experimental data for WSe_2, while the lines depict the fit to an exponential function. (a)–(d) are adapted with permission from Ref. [125], © Lien, D.-H. et al. 2018. (e)–(g) are adapted with permission from Ref. [126], © WILEY-VCH Verlag GmbH & Co. KGaA, Weinheim 2019. (h)–(j) are adapted with permission from Ref. [127], © Paur, M. et al. 2019.

3 Light emitting applications based on two-dimensional perovskite material

Perovskite has currently attracted great attention in both the academic and industry fields as a potential candidate for next generation of optoelectronic devices. Compared to its conventional three-dimensional counterpart, two-dimensional perovskite films have gained more interest because of their unique structural characteristics and distinct performance. Although the 3D organometal halide perovskites have been widely applied into optoelectronic applications due to their outstanding electrical and optical properties, including broad and strong absorption spectrum, long charge diffusion length, high carrier mobility and long carrier lifetime [128, 129], the crystal-lattice of such bulk perovskite could be easily damaged if exposed to high temperature, high humidity environment and ultraviolet irradiations. The decomposition of perovskites would be accelerated due to these special conditions, resulting in the generation of some reactants that rapidly degrade the performance of related devices [128]. Perovskite based

applications usually require high performance devices, such as photodetectors, solar cells, field effect transistors and light-emitting diodes. The performance of these devices highly depends on the perovskite material properties [130]. Therefore, more attractive 2D films with higher humidity resistance, smaller grain size and better surface coverage should be further developed [129], which would be a better approach with considerable humidity and temperature stability for use in optoelectronic applications [128].

3.1 Preparation methods

High quality materials are desired for high efficiency devices. Many researchers have proposed several different methods to synthesize high quality 2D perovskite thin films with inspiration of the synthesis routines of traditional 3D perovskite crystals [131]. In this section, the process of some common synthesis routines of 2D perovskite will be reviewed in detail.

3.1.1 Spin-coating

The one-step spin coating method has been widely employed to fabricate 2D perovskite materials, owing to its low cost and simple process. The majority of reported 2D perovskite films are mostly prepared by this method, which is straightforward with further enrichment needed [128]. The first step of this method is to obtain the precursor solution, and then different dimensions and morphologies of perovskites could be obtained by adjusting the ratio of precursors [132]. To be more specific, this precursor solution is normally formed from dissolving organic halide AX and bivalent metal halide BX_2 (PbI_2, $PbBr_2$, or $PbCl_2$) in organic solvents, which are then transferred onto different matrices or substrates with annealing to form the thin films by spin casting or dropping [133], as shown in the Fig. 9(a). For different targeted or required crystallinity of perovskite films, the working temperature and processing time are important for high quality final products. Meanwhile, the concentration and composition of precursor solution should be also considered before selection [133]. Some research examples are presented here.

In 2010, Gauthron et al. reported that $(PEA)_2PbI_4$ thin films were obtained by dissolving $(C_6H_5C_2H_4NH_3)_2I$ (PEAI) and PbI_2 in dimethylformamide (DMF), and then the solution was spin coated onto a quartz substrate [134]. However, the thickness of those films that are generated by the same way varies from 3 to 100 nm, which results from different precursor concentrations and spin-coating speeds. Recently, Gao et al. has also prepared the 2D hybrid perovskites from a ternary mixed solvent using a similar fabrication method, which was reported by Dou et al. in 2015 [135]. The crystal structure of the prepared 2D perovskites was resolved using single-crystal X-ray diffraction with side views shown in Figs. 9(b)–9(d) for $(2T)_2PbI_4$, $(4Tm)_2PbI_4$ and $(BTm)_2PbI_4$, respectively. The corresponding optical microscope images are shown in Figs. 9(e)–9(g) with an inset showing their single quantum wells structures. The authors pointed out that a dilute precursor solution was spin coated onto a Si/SiO_2 substrate or glass slide at 2,000 rpm to produce $(4Tm)_2PbI_4$ thin films, then heated in nitrogen at 200 °C for 10 min [131]. All other hybrid perovskite thin films were prepared using a similar procedure but with different thermal annealing temperature. Specifically, the $(2T)_2PbI_4$ formed the desired perovskite phase immediately after solvent evaporation, while the $(BTm)_2PbI_4$ thin films were annealed at 120 °C [131]. They further noted that these two-dimensional sheets were generated with well-defined square shapes and the lateral sizes are approximately 10–20 μm. The thickness and layer numbers were confirmed by atomic force microscopy (AFM) images, indicating a range of 2–8 nm, as shown in Figs. 9(h)–9(j). In order to get the uniform and smooth surface of thin films, the DMF and chlorobenzene (CB) co-solvent were initially investigated. Dropping of this antisolvent (CB) during the spin-coating process would immediately form the homogeneous nuclei with growing up slowly [136]. The CB helps to reduce the solubility of materials in DMF thereby promoting crystallization. Since the boiling point and evaporation rate of CB are similar to those of DMF, the drying and crystallization process of solvent could be uniform across the entire substrate [48]. Dou et al. suggested that acetonitrile was also introduced to form the ternary mixed solvent to assist the formation of the ultrathin and uniform square shaped 2D hybrid perovskite sheets on the substrate due to the faster evaporation rate of acetonitrile [48]. This solvent has also been used and demonstrated by Mercier et al. in 2004 to fabricate perovskite single crystals via the spin-coating technique [137]. For a similar purpose, Liang et al. introduced solvent vapor annealing technique in combination with spin-coating to prepare $(PEA)_2PbBr_4$ thin films [138]. The authors stated that solvent vapor annealing is a crucial step to successfully obtain 2D layered perovskites with increased grain size. It has been used to convert polycrystalline $(PEA)_2PbBr_4$ thin films into high-quality micro-sized nanoplates, which enhanced both the optical properties and the external quantum efficiency of the 2D perovskite based LEDs [138]. They further stated that the thickness of the nanoplate that is created by this treatment was highly dependent on the spin-coating speed and the concentration of the precursor solution [138]. This solvent vapor annealing technique has also been employed with toluene [139] solution, and has been successfully used to spin-coat onto non wetting substrates [140] to improve the crystallinity of organometal lead halide perovskites. Specifically, Liang et al. mainly reported high-quality two-dimensional $(PEA)_2PbBr_4$ perovskite, which was obtained by spin-coating a DMF solution of phenethylammonium bromide (PEABr) and $PbBr_2$ (2/1) on the indium-tin oxide (ITO)/poly(3,4-ethylenedioxythiophene):polystyrenesulfonic acid (PEDOT:PSS) substrate [138]. After that, the authors placed the sample face down on the edge of the glass dish without contacting it. The dish was then transferred to a covered beaker with DMF, forming a closed space with DMF vapor. The temperature of the DMF solvent was maintained at 30 °C for a few minutes, which allowed the DMF vapor diffuse under the $(PEA)_2PbI_4$ membrane and react with it. When the film turned purple, it was immediately removed and baked at 100 °C for 10 min. Through this DMF vapor annealing, the small and dense $(PEA)_2PbI_4$ perovskite grains recrystallized into micro-sized nanofilms uniformly distributing onto the substrate. These films have larger grain size, higher crystallinity, and higher PL strength, which are promising for LEDs applications.

However, the materials obtained by this method still cannot fully exhibit the nature of perovskite, because it sometimes shows inhomogeneous, polycrystalline structures and large surface roughness. In order to obtain a more uniform, smooth, homogeneous, and high crystalline two-dimensional perovskite, the method of thermal evaporation is proposed. It may need dedicated equipment, and it is also hard to avoid the PbI_2 vapor during the experiment process [130].

3.1.2 CVD growth

CVD is a favourable deposition method for the preparation of high-quality 2D perovskites with well-defined structure and morphology [141]. It is mainly based on the theory of evaporation from gas phase, using gas as the deposition materials and conducting chemical reactions in a high vacuum

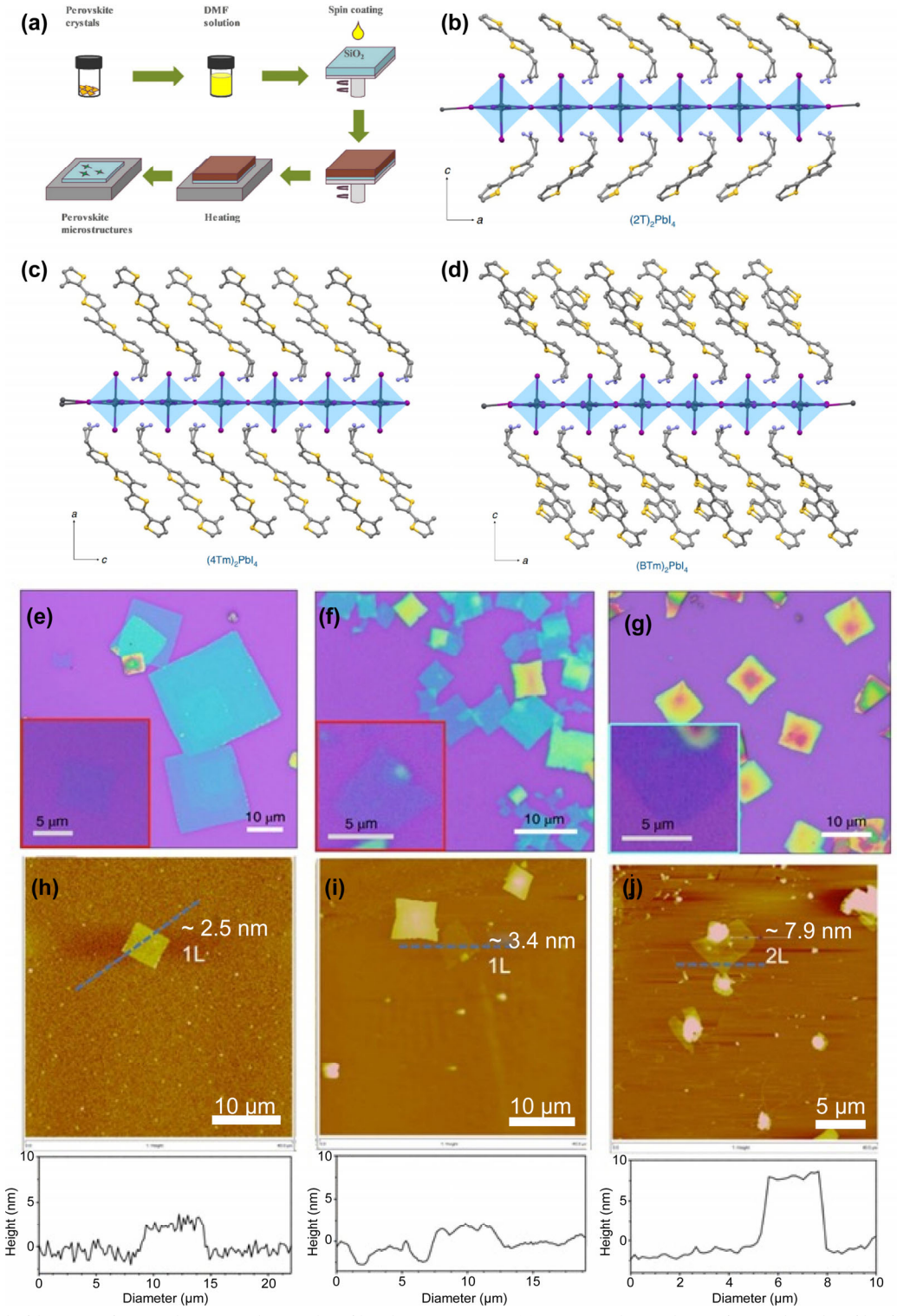

Figure 9 Sample fabrication for two-dimensional Perovskite films by spin-coating. (a) Stages in the synthesis of perovskite thin film from spin coating technique. (b)–(d) The chemical structure of $(2T)_2PbI_4$ (b), $(4Tm)_2PbI_4$ (c) and $(BTm)_2PbI_4$ (d) 2D sheets, where purple is I; yellow represents S; blue is N; grey is C and blue diamonds within inorganic layers represent octahedral $[PbI_6]^{4-}$; H atoms were removed for clarity. (e)–(g) Optical image of the 2D sheets ($(2T)_2PbI_4$ (e), $(4Tm)_2PbI_4$ (f) and $(BTm)_2PbI_4$ (g)) grown on SiO_2/Si substrate. Scale bar is 10 mm. The insets are corresponding images for monolayer-thick single-quantum-well structures. (h)–(j) AFM images and height profiles of molecularly thin perovskite films. The thickness is around 2.5, 3.4 and 7.9 nm for $(2T)_2PbI_4$ (h), $(4Tm)_2PbI_4$ (i) and $(BTm)_2PbI_4$ (j) respectively. (a) is adapted with permission from Ref. [133], © The Royal Society of Chemistry 2018, (b)–(j) are adapted with permission from Ref. [135], © Gao, Y. et al., under exclusive licence to Springer Nature Limited 2019.

environment to fabricate thin films [142]. In recent years, this method has been attempted and widely reported for the synthesis of 2D perovskites.

Tavakoli et al. stated the specific fabrication process of perovskite thin films by using CVD tube furnace, and the schematics is shown below in Fig. 10(a) [143]. To be more specific, the thin films obtained were deposited on top of a c-TiO_2-coated fluorine doped tin oxide (FTO) glass substrate by a one-step method. As can be clearly seen from the figure, $PbCl_2$ or PbI_2 and methylamine iodide (MAI) were firstly located in the high temperature zone and the specific position of each source was determined based on its particular vaporization

temperature. The substrates were normally placed in the low temperature zone during the process of growth, allowing the vapor to pass through with the change of temperature and the assistance of carrier gas. After heating the source, the perovskites were deposited on the substrate, while an argon carrier gas was used for the MAI and PbX_2 vapors at a flow rate of 70 s ccm [143]. The morphology of the perovskite thin films obtained by this method was evaluated by scanning electron microscopy (SEM) (Fig. 10(b)) and AFM (Fig. 10(c)). From the SEM image, the authors pointed out that the synthesized perovskite films have large grain size up to micron scale with good surface coverage, and the AFM images estimated the root-mean-square (RMS) surface roughness of perovskite films to be 43 nm in the region of 10 μm × 10 μm, which is similar to the roughness of the films fabricated through other evaporation methods [143]. A number of parameters could be optimized, such as processing time, heating temperature, annealing process or source position for further improvement of the films. Furthermore, Liu et al. also found that organometal halide perovskite thin films prepared by this dual-source ($PbCl_2$ and MAI) vapor deposition method were much more uniform and homogeneous than the films fabricated by spin-coating process [144]. However, the perovskite films via this facile one-step method mentioned above were still relatively thick, being on the order of several hundred nanometers. In 2014, Ha et al. reported the synthesis of 2D $MAPbI_3$ perovskites by two-step vapor deposition [145]. Firstly, with epitaxial growth, the PbX_2 nanoplatelets were grown on a mica substrate, and then the lead halide nanoplatelets were transformed into perovskites with methylammonium halide molecules using gas–solid hetero phase reaction. The lateral dimension of nanoplates was controlled from 5 to 10 μm, the thickness of perovskite platelet was controlled by adjusting the thickness of lead halide platelets, which also varied from tens to hundred nanometres [145]. Similar work has been demonstrated in other groups with Wang et al. (2015) pointing out that van der Waals force is a key parameter in the growth of single crystal large sized 2D perovskites [146]. The ionic crystals with localized bonds are more tended to form ultra-thin structures than covalent compounds with localized bonds. Liu et al. also prepared 2D $MAPbI_3$ nanoplatelets by two-step CVD growth, but the films they obtained were different from those reported by Ha et al., and the thickness of these nanoplatelets was as thin as that of a single unit cell [141]. Firstly, they obtained ultra-thin PbI_2 nanoflakes by casting the saturated aqueous PbI_2 solution onto a substrate and continuously heating the substrate at an elevated temperature. The atomically thin $MAPbI_3$ flakes were then achieved in a CVD system by the chemical conversion of ultra-thin PbI_2 flakes [141]. Figure 10(d) depicts the synthesis process and AMF images are shown in Figs. 10(e)–10(h) confirming that $MAPbI_3$ flakes with the thickness of 1-, 2-, 4-, and 10-layer were obtained by utilizing this method. This two-step process is very versatile and can be used to prepare various 2D halide perovskite nanostructures by inserting different organic cations or halide anions. Two-dimensional $MAPbI_3$ nanosheets exhibit high PL quantum yield, while the emission shows a red shift when the thickness of nanosheets increases, which may resulted from lattice expansion [142].

CVD method has obvious advantages in fabricating 2D perovskites, including controllable thickness, smooth surface, high crystallinity and few impurities and defects. However, the coverage and quality of products need to be improved, and some other more appropriate as well as efficient preparation methods are still expected to be developed.

3.1.3 *Other common techniques*

In addition to these two popular techniques mentioned above, a few other methods including simple solution method, dip

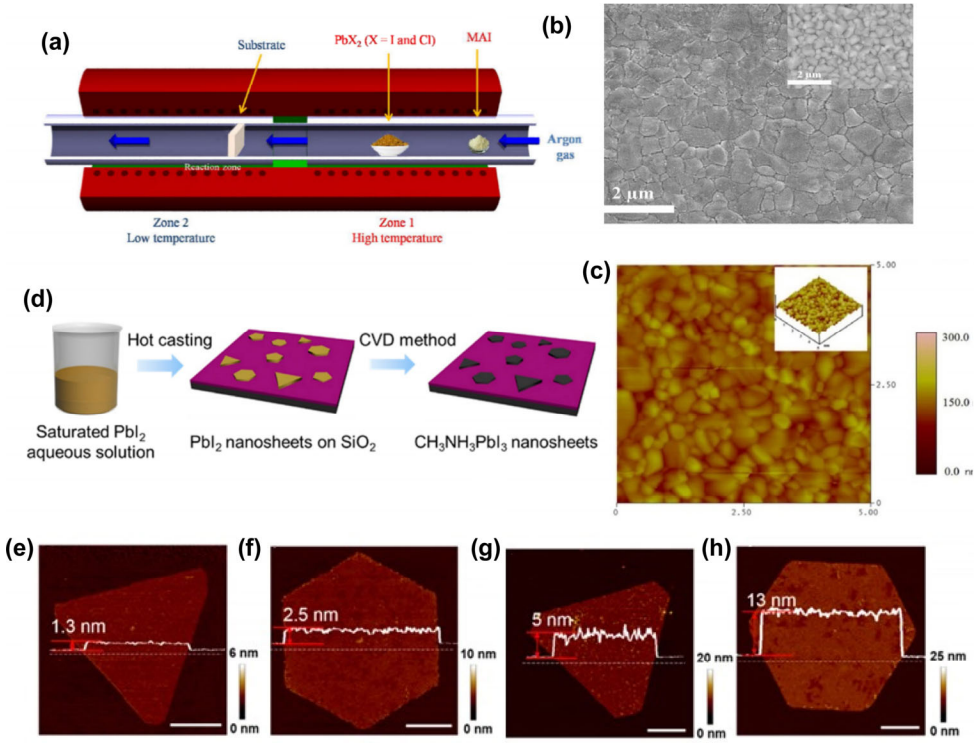

Figure 10 Sample fabrication for two-dimensional perovskite films by CVD growth. (a) Schematics of the perovskite film fabrication process in a CVD furnace. (b) Top-view secondary electron SEM image of a $CH_3NH_3PbI_{3-x}Cl_x$ layer, the inset shows backscattered electron image with higher resolution. (c) AFM image with an inset showing the 3D topographic image. (d) Schematic illustration of two-step CVD process to fabricate 2D $CH_3NH_3PbI_3$ perovskite nanosheets. (e)–(h) AFM images of 2D $CH_3NH_3PbI_3$ nanosheets with different thicknesses. Scale bar is 2 μm. (a)–(c) are adapted with permission from Ref. [143], © Tavakoli, M. M. et al. 2015. (d)–(h) are adapted with permission from Ref. [141], © American Chemical Society 2016.

coating and hot casting are widely used as well in the research field. The solution method is a simplified coating technique without other processing procedure like spinning, which is reported by Dou et al. in 2015. The molecularly thin 2D hybrid perovskite (with mainly n = 1) was obtained for the first time by this method, using the same ternary co-solvent of chlorobenzene, dimethylformamide and acetonitrile to control the solute solubility and solvent evaporation speed [41]. The solution was firstly drop-casted onto a Si/SiO_2 substrate and dried under a mild temperature of 75 °C to precipitate uniform squaresheets [41], and the whole process is schematically shown in Fig. 11(a). From this experience, it is realised that the solubility of the precursor should be kept continuously low so that the solutes do not concentrate during the solvent evaporation [147]. Although Dou et al. prepared good quality films by using solution method, Leng et al. pointed out that this method is very simple, fast and convenient to generate perovskites, while the major disadvantages include thickness inhomogeneity, the small size of the crystallites and flake aggregation that are usually challenging to avoid and control [148].

Another similar method is dip coating, which normally involves the process of immersing a substrate into the solution, and then removing it from the tank to allow draining. Koh et al. reported this method for fabricating $(IC_2H_4NH_3)_2(CH_3NH_3)_{n-1}Pb_nI_{3n+1}$ quasi-2D perovskite films, and the procedures of dipping process is illustrated in Fig. 11(b) [149]. Firstly, a pure 2D perovskite $(IC_2H_4NH_3)_2PbI_4$ layer was deposited by spin coating of the precursor solution, and the substrate was subsequently immersed into MAI solution with a certain concentration for various dipping duration (1–5 min), to increase the stacking order and convert the films into a higher dimensionality($1 < n < \infty$), as indicated in Fig. 11(b) bottom inset [149]. With increasing dipping time, more methylammonium (MA^+) cations in solution permeate into $(IC_2H_4NH_3)_2PbI_4$ films thus the thickness of inorganic PbI_4 layers will be increased [128]. This is a good way to fabricate nanostructured mixed-dimensionality perovskites films by controlling the dipping time, but the improvements in controlling surface coverage and effective blocking layer deployments are required, and the withdrawing speed will easily affect the generated films [149].

In addition, a new hot-coating method is proposed in order to achieve high-quality perovskite films, which is basically an advanced version of spin-coating, and the key point of which is to precisely control the temperature of the substrates. In 2016, Tsai et al. reported that 2D perovskite solution was prepared by dissolving 2D $(BA)_2(MA)_{n-1}Pb_nI_{3n+1}$ single crystal in DMF, and the solution was heated under continuous stirring at 70 °C for 30 min before coating [51]. After that, FTO/PEDOT:PSS substrates were preheated for 10 min from 30 to 150 °C, and the precursor solution was spin coated on the hot substrate at a speed of 5,000 rpm. for 20 s. Figures 11(c)–11(f) demonstrated the AFM and SEM images for the films obtained by hot coating and room temperature spin coating, showing that hot coating films are not only larger in grain size, resulting in an uniform and compact film, but also hold a smaller pinhole density [51].

Compared with the solution method and dip coating, spin coating technique and CVD growth allow for better controllability of the size, shape, and composition of the 2D halide perovskite films. However, there is still room for further improvement, and more precise and advanced techniques based on these basic methods such as hot coating are expected,

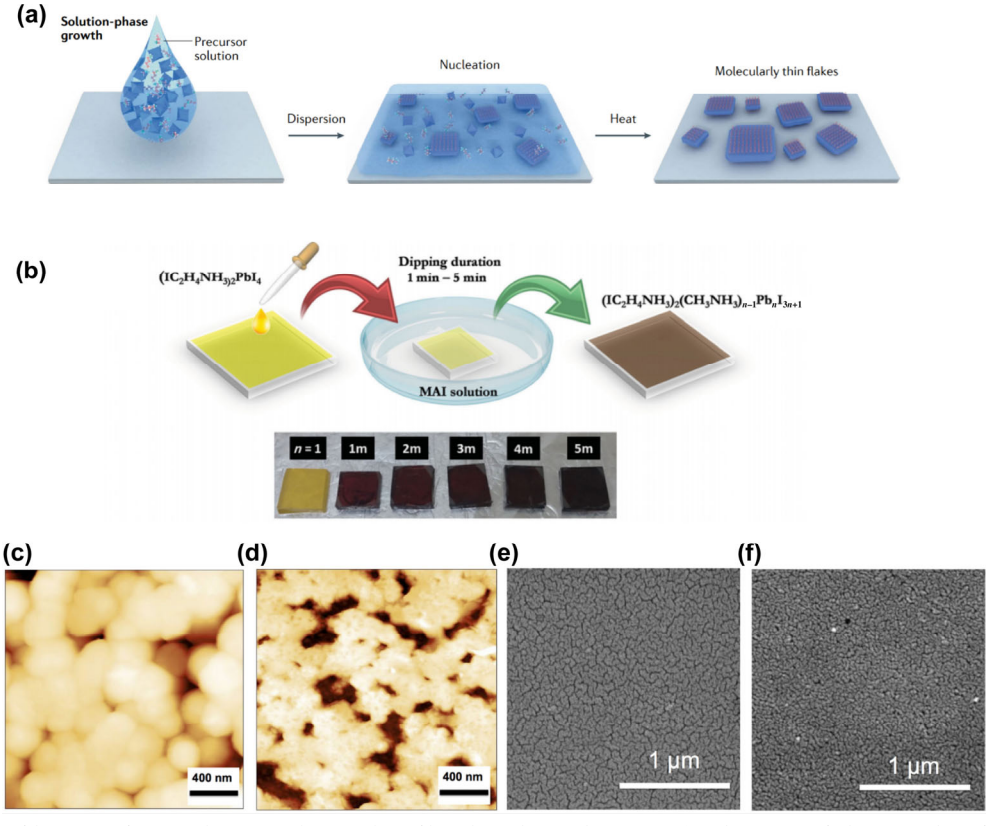

Figure 11 Sample fabrication for two-dimensional perovskite films by other techniques. (a) Schematics of the perovskite film fabrication by solution-phase growth method. (b) Schematic illustration of fabrication of perovskite thin films and the photographs of the perovskite films deposited in different dipping time, from 1 to 5 min. (c) and (d) AFM images of surface morphology for hot-coating (c) and room-temperature spin-coating (d) films. Scale bar is 400 nm. (e) and (f) SEM images of topography for hot-casting (e) and room-temperature-casting (f) films. Scale bar is 1 μm. (a) is adapted with permission from Ref. [148], © Springer Nature Limited 2020. (b) is adapted with permission from Ref. [149], © WILEY-VCH Verlag GmbH & Co. KGaA, Weinheim 2016. (c)–(f) are adapted with permission from Ref. [51], © Macmillan Publishers Limited, part of Springer Nature 2016.

which should combine all advantages of current methods and be able to produce good quality 2D perovskites with simple fabrication methods and low cost.

3.2 Properties of 2D perovskites

Due to the superior luminance properties of 2D perovskites, it has attracted great attentions for various applications, not only used in the field of solar cells but also light emitting devices. 2D perovskite materials are developed as one of the alternatives for optoelectronic applications with considerable humidity and temperature stability as well as enhanced excitonic properties. These outstanding optical properties are mainly related to their structure, as the 2D perovskites is characterized by inserting organic layer crystals between inorganic substances [128]. This section will briefly introduce the structure of 2D perovskites and summarize the merits of 2D perovskites over its 3D counterpart in the perspective of optoelectronic properties.

3.2.1 *Structure*

Two-dimensional perovskites were firstly investigated and studied in 1989. Ishihara et al. reported that the thickness of 2D perovskite is similar to that of only one or a few atomic layers because of the dimensional confinement [150]. The electron–hole pairs are easily confined to a plane due to strong Coulomb interactions. There are normally two kinds of 2D perovskites, which are distinguished by their geometric structure. The most traditional one is featured by 2D geometric nanostructure form, such as nano-plates, nano-sheets or nano-disks, which are mainly obtained by limiting the growth alone different crystal planes. This type of perovskite has been named as 2D ABX_3 perovskite, and its thickness is controlled at atomic scales [151]. While another type is featured by a lamellar crystal structure and crystal stacking, the most common one is Ruddlesden-Popper (RP) phase layered perovskite which has been widely reported [131]. Structurally, the metal halide $[BX_6]^{4-}$ octahedral units are connected into a corner-sharing halide anions for 3D perovskite, and the voids are occupied by A cations within the framework, as shown in Fig. 12(a) [152]. However, when A is replaced by large organic cations, they would not fit into the gap between the $[BX_6]^{4-}$ octahedral units, and the framework will be constrained to form the two-dimensional structure. Therefore, 2D shows the different characters in comparison to the 3D perovskites [153]. The RP phased perovskites are generated from 3D structures, as shown in the Figs. 12(b) and 12(c), which are formed by splitting 3D perovskite along lattice orientations of <001> and <110> [154]. The general chemical formula of RP phase is $(A')_2(A)_{n-1}B_nX_{3n+1}$, where A′ is R–$NH_3$ or H_3N–R–NH_3 and R is a large aromatic ligand or aliphatic alkyl chain. This component works as an insulating layer to isolate different inorganic layers that are shared by metal halide octahedral units through corner atoms. A refers to a monovalent cation such as Cs^+ or MA^+. B is a divalent heavy metal cation like Pb^{2+} or Sn^{2+} and X represents a halogen anion such as Cl^-, Br^- or I^-. Symbol n represents the number of monolayer metal halide sheets between the insulating A′ organic layers [128]. At $n = \infty$, the corresponding perovskites have conventional 3D structures, when n = 1, 2, 3, etc., a few layers (n) of octahedra will be sandwiched by two layers of cations with many adjacent stacking layers induced by van der Waals forces. However, when n = 1, this perovskite would have a strict 2D structure [155], and when n = 2–5, it seems to be quasi-2D structure [128]. Sun et al. reported the perovskite with multiple quantum wells structure to achieve the high efficiency and stable perovskite LEDs [156]. This multiple quantum wells (MQW) perovskite is a mixture of layered perovskites with different band gaps generated from various layer numbers (n) of lead halide [156], thus from quasi-2D structure. They pointed out that this structure could combine the advantages of both pure 2D perovskites and 3D perovskites, as it has a smooth film morphology similar to the pure 2D perovskite film [157, 158] but it could have higher photoluminescence quantum efficiency because of the fast energy transfer from large band gap QWs to small band gap QWs where efficient emission occurs [158]. The structure of materials plays a significant role in affecting the performance of their related devices, as the number of inorganic layers influences not only the optoelectronic properties but also the crystal formation and orientation of 2D perovskites [159]. For example, when n = 1 for $BA_2MA_{n-1}Pb_nI_{3n+1}$, the structure and intrinsic anisotropy of the 2D materials cause in-plane growth, and the orientation of layers is parallel to the substrate [160]. In contrast, when n = 4, the two-dimensional crystals grow in a more random orientation, with the preferred orientation being perpendicular to the substrate [161]. Chen et al. pointed out that aligning the 2D perovskite layers perpendicularly to the electrodes is desirable for efficient LEDs, as the organic cations are electrically insulating, and charge transport may be easily hindered in the parallel configuration while vertical stacking could provide a direct pathway for electron and hole transport through the perovskite [162]. Hence, the quasi-2D perovskite could be the preferred structure for later applications.

3.2.2 *Optical properties*

In order to apply the perovskite as an optical active layer for light emitting to obtain high efficiency LEDs, the luminous efficiency of materials is the first priority to be explored, and it will be essential to optimise this optical property by adjusting its structure. The excellent enhancement of 2D perovskites' properties compared to bulk perovskites makes them to be extraodinary luminescent materials for light-emitting diodes [132].

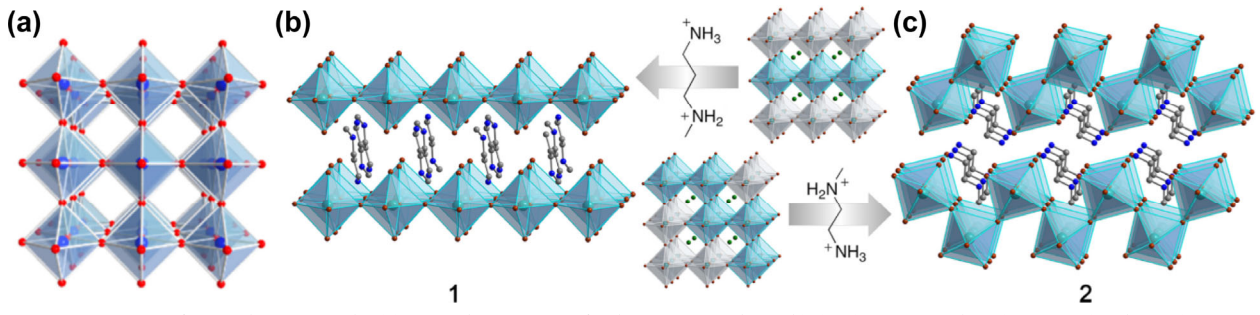

Figure 12 Structure of perovskite materials. (a) Crystal structures of cubic 3D perovskite. (b) (001) 2D perovskite (N-MPDA) [$PbBr_4$] (N-MPDA = N'-methylpropyl-1,3-diammonium). (c) (110) 2D perovskite (N-MEDA) [$PbBr_4$] (N-MEDA = N'-methylethane-1,2-diammonium). (a) is adapted with permission from Ref. [152], © American Chemical Society 2018. (b) and (c) are adapted with permission from Ref. [154], © American Chemical Society 2014.

3.2.2.1 *Quantum confinement and Exciton properties*

Similar to other two-dimensional materials, the 2D perovskite also exhibits the quantum confinement effect, and the exciton binding energy of 2D perovskites is largely impacted by dielectric environment and quantum confinement effect than that of 3D counterparts [163]. Generally, the dielectric constant of organic layers is much smaller than that of inorganic layers, therefore, the Coulomb interaction of the electron and the hole will be strongly enhanced in 2D perovskites. Kumagai and Takagahara (1989) have reported that the Coulombic force between electrons and holes is largely enhanced in 2D perovskites due to the dielectric quantum confinement and small shielding effect, implying that the perovskites are excitonic materials with larger electron–hole binding energy [164]. The authors also pointed out that the exciton binding energy of 2D perovskites could be theoretically enhanced up to 100 times higher comparing with 3D materials. However, the actual exciton binding energy of 2D perovskites is at most several hundred meV lower than the theoretical prediction, which is only tens of meV higher than exciton binding energy in 3D perovskites. The binding energy of quasi-2D perovskites exciton is intermediate between 2D and 3D perovskites. More specific data for binding energy of perovskites with different structures are displayed in Table 1. Therefore, based on the structure theory explained above in the previous section, it is noticed that the exciton binding energy could be increased by inserting various larger organic cations. In addition, Dou stated that large exciton binding energy would be beneficial to radiative recombination and consequently the higher PL quantum yield would be easier to be achieved. Then the material will be more suitable for the devices that work mainly based on electron–hole recombination, such as light emitting diodes [165]. Furthermore, it has been reported that the 2D perovskite has a wider band gap [166] and a more narrow photoluminescence spectrum [48] compared with the 3D perovskite, and the bandgap of material could be easily tuned by adjusting the thickness of that inorganic layer. As symbol n increases, the excitonic properties of 2D perovskites will be correspondingly weakened, and then show a transition from semiconducting to metallic behaviour [167].

3.2.2.2 *Charge transfer*

Ma et al. (2018) stated that the 2D perovskite could be served as a quantum-well structure due to its spatial-confinement layered nanostructures with the organic layers acting as barriers and a built-in electric filed between the negative and the positive inorganic layer [128]. It is generally known that the excitons for III-V group's semiconductors like GaAs, GaAs and AlAs could only exist stably at extra low temperature [168], while excitons of 2D perovskite can be observed at room temperature because of the Coulomb medium shielding effect [169].

Table 1 Exciton binding energy of different structure perovskites

Dimensional networked	Composition	Binding energy (meV)
3D	$MAPbX_3$	~ 19–76 [192–194]
3D	$MAPbI_{3-x}Cl_3$	55 ± 20 [195]
3D	$CsPbBr_3$	42 [196]
2D	$(C_6H_5C_2H_4NH_3)_2PbI_4$	~ 220 [163]
2D	$(C_4H_9NH_3)_2PbBr_4$	480 [197]
2D	$(R)_2Pb_nBr_4$ (R = BA, PEA, PBA)	310–320 [198]
Quasi-2D	$(MAPbI_3)(C_6H_5C_2H_4NH_3)_2PbI_4$	170 [163]
Quasi-2D	$CsPbX_3$ NPLs	120 [199]

There may be a mismatch of dielectric-constant between inorganic layer and organic layer, resulting in enhanced exciton performance in 2D perovskite. Byun et al. (2016) suggested that some quasi-2D perovskite films are in multiple phases of mixed dimensions rather than the single phase like pure 2D perovskite [170], which could be revealed by their absorption spectra at room temperature (Fig. 13(a)). The several different dominated peaks in the spectra imply that the films contain different quasi-2D perovskite crystals with different dimensions. For the pure perovskite (when n = 1), there is only one phase and it is named as P1, and the corresponding absorption spectrum is shown in Fig. 13(b) and it shows only one peak for n = 1 [136]. When n is small, the phases P1, P2 and P3 will be dominated, while when n is increased to be 2, 3, 4, etc., the quasi-2D perovskites exhibit different crystal phases with various dimensions, corresponding to several absorption peaks in Fig. 13(b). In Fig. 13(c), the overlapping PL peaks originated from quasi-2D perovskite films are located at around 520 nm. However, the pure 2D perovskite has different peak position at around 410 nm, which is about 110 nm difference [170]. This also further implies the multiple phases in quasi-2D perovskite films. It has been noticed that the PL peak positions of quasi-2D perovskites are almost at the same position as those of 3D perovskites, which is related to exciton confinement and photo-excitation transfer along different phases. The PL is produced by the phase with the smallest band gap, as shown in Figs. 13(d)–13(f). Furthermore, Wang et al. stated that the self-organized multiple quantum wells in some quasi-2D perovskite films with different exciton energies were found aligned in a certain tendency, like the cascade energy transfer shown in Fig. 13(g). It clearly indicates that excitation energy is transferred downstream from small-n QWs to large-n QWs, with emission mainly coming from the larger-n QWs. Besides, Yuan et al. suggested that the multiple phases of mixed dimensions work as a carrier concentrator in some quasi-2D perovskite films, and it could offer a funnel mechanism for the transportation of excited carriers [171]. This fast energy transfer limits the quenching effect of excitons and facilitates effective radiation recombination in large-n quantum wells with better emission performance resulting in the improved performance of perovskite LED [158]. Figure 13(h) shows the light-intensity dependent PL quantum efficiency (PLQE) of the $NFPI_7$ MQW film under 445 nm continuous wave laser excitation, the high PLQE of up to 60% indicating that the photogenerated excitons in small-n quantum wells could be energy transferred to the large-n quantum wells with excellent emission characteristics for effective radiative recombination [158]. More importantly, it is worth noting that the MQW films could exhibit high PLQE at an excitation as low as about 0.3 mW/cm^2, which is obviously different from that of the bulk 3D perovskite films [158]. Typically the bulk perovskite presents high PLQE at very high excitations. For example, Felix Deschler et al. reported above 65% PLQE when excitation power exceeded 500 mW/cm^2 [172].

3.2.2.3 *Superior stability*

In comparison with the traditional 3D perovskites like $MAPbI_3$, 2D perovskite films and quasi-2D perovskite films would show the enhanced environmental and thermal stability due to several major factors and multiple interaction forces in 2D perovskites. These include strong ionic and covalent bond within inorganic layers, weak van der Waals force within organic layer, and connections between organic and inorganic layers. For instance, the coordination bonds between ammonium group and Pb, hydrogen bond between ammonium group and halogen [128]. Compared to the structure of 3D perovskites,

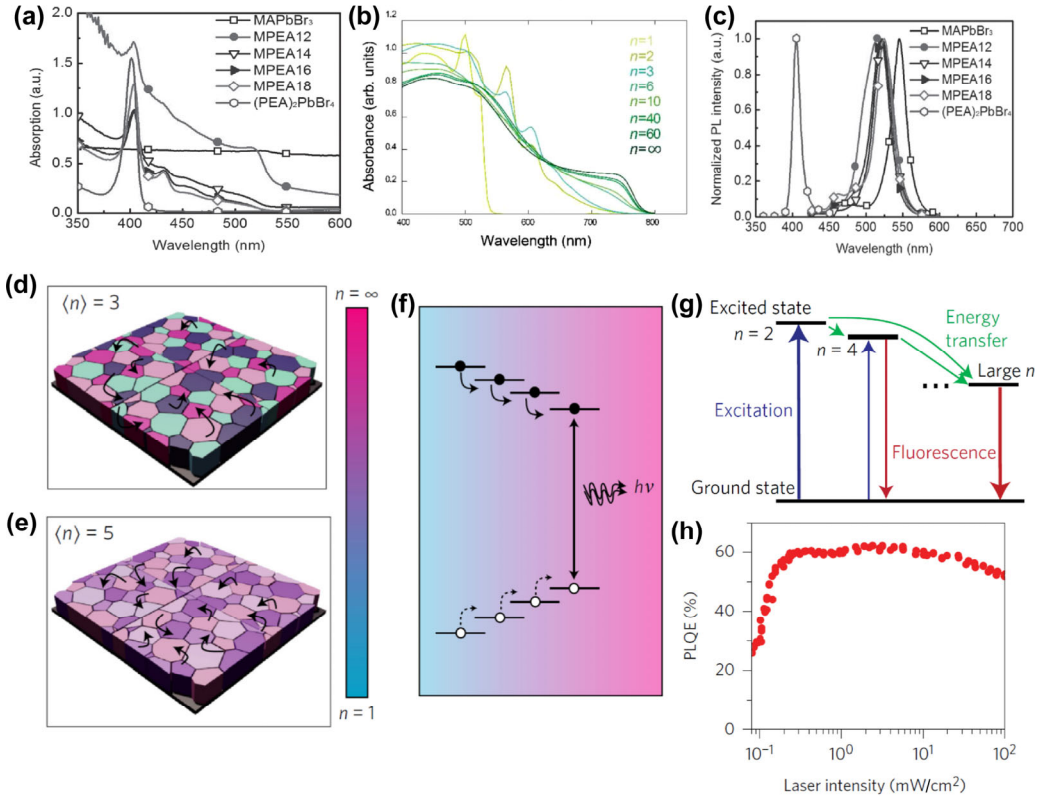

Figure 13 Energy transfer in quantum-well-structured 2D perovskite. (a) Absorption spectra of different quasi-2D perovskite films on glass substrate. (b) Absorption spectra of the perovskite films with different n values. (c) PL spectrum of quasi-2D perovskite films. (d) The carrier transfer process in n = 3 perovskite. (e) The carrier transfer process in n = 5 perovskite. (f) Energy transfer across an inhomogeneous energy landscape in multi-phase perovskites, concentrating carriers to smallest bandgap emitters. The arrows represent the carrier transfer process. (g) Schematic of cascade energy transfer in MQWs. (h) Excitation intensity dependent PLQE of the MQW film. (a) and (c) are adapted with permission from Ref. [170], © WILEY-VCH Verlag GmbH & Co. KGaA, Weinheim 2016. (b) is adapted with permission from Ref. [136], © American Chemical Society 2016. (d)–(f) are adapted with permission from Ref. [171], © Macmillan Publishers Limited, part of Springer Nature 2016. (g) and (h) are adapted with permission from Ref. [158], © Macmillan Publishers Limited, part of Springer Nature 2016.

there are organic cations in 2D perovskite films, which could extend into a wider space under of van der Waals forces. Therefore, a higher energy is required to interrupt interaction between the large-group ammoniums and inorganic layers in 2D structure than in 3D structure with MA^+ cations or formamidinium ion (FA^+) cations [173]. Additionally, Smith et al. indicated that the hydrophobic organic side chains in 2D perovskites layered structures could act as a protective shell to against moisture in the air and prevent inorganic crystals from being damaged [174]. Mitzi et al. also suggested that the strong van der Waals interactions between the capping organic molecules could also improve the stability of material [167]. The density functional theory (DFT) simulation has been conducted by Quan et al. revealing that the decomposition reaction of perovskite crystal begins spontaneously from the surface of material instead of inside the crystal [136]. The authors also pointed out that the removal of large organic molecules from the 2D perovskite films needs around 0.36 eV higher energy than the removal of small organic molecules from 3D perovskites. Accordingly, desorption rate of organic cations is decreased by 6 orders of magnitude while film decomposition process is slowed down by a factor of 1,000 [136]. An example here is that the 2D PeSCs remained stable in air after several months, but the 3D counterpart has begun to degrade after just a few days [128]. Moreover, suppressed ion migration in 2D perovskites is another main contributing factor for their superior stability, as it would promote the decomposition of 3D perovskites and degradation of optoelectronic properties [173, 175]. Lin et al. indicated that the organic layers in 2D perovskite could effectively prevent ion migration along the out of plane direction [176] and mitigate the related degradation processes [51]. The temperature dependent conductivity measurement was conducted to investigate the ion migration along in plane direction [51], and authors found that the energy needed to form iodide vacancies and methylammonium vacancies in layered perovskite like $BA_2MA_2Pb_3I_{10}$ (n = 3) are quite larger than that in 3D perovskite $MAPbI_3$, implying that the formation of defects in quasi-2D perovskites is more difficult than the 3D counterpart. Therefore, the vacancy sites available for ions to migrate are largely reduced. As a result, ion migration along the direction of current conduction is also inhibited in 2D perovskite, which further improves the stability of devices [177].

Recently, 2D and quasi-2D perovskites have receive much attention as the light-emitting materials to enhance the luminescent efficiency of the perovskite LED (PeLED), because of their excellent performance, including effective exciton recombination, high quantum yield, as well as improved thermal stability. These advantages provide 2D perovskites big potential for optoelectronic applications in related devices. Yang et al. has emphasized that the external quantum efficiency of the halide perovskite LED is significantly enhanced by up to 14.36% with quasi-2D perovskites as emitters [178].

3.3 Application in light-emitting diodes

Nowadays, organic-inorganic hybrid perovskites have been intensively studied in LEDs due to their high PL efficiency and wide colour ranging from visible to near-infrared. The considerable

efforts have been devoted to improving the performance of perovskite LED by introducing 2D perovskite emitter layers. From a fabrication perspective, layered 2D perovskites show good film processability with the excellent optical properties. Some results have been published recently on 2D or quasi-2D perovskite-based LEDs.

In 2016, Xing et al. fabricated LED devices using amorphous $CH_3NH_3PbBr_3$ nanoparticles as the light emitting material, and the LEDs show a maximum current efficiency (CE) of 11.49 cd/A, a luminous efficiency of 7.84 lm/W and an external QE of 3.8% [179]. Although, the 3D perovskite LEDs benefit from high colour tunability owing to varying proportion of halogen ingredients, the performance of 3D perovskite LEDs is limited by the fact that 3D perovskites usually show the small exciton binding energy but a long exciton diffusion length [180]. The excitons in 3D perovskites could be easily dissociated into carriers and then quenched by defects, hindering radiative recombination and causing negative effects on EL efficiency. Tan et al. stated that the light emitting layers of LEDs are usually thin which could limit the carriers injection and thus maximise the charge density [181]. However, there are pin holes on thin films thus the coverage of substrates is sometimes incomplete, resulting in moderate external quantum efficiency [182]. To solve this issue, the effective method is to reduce the size of perovskite so that excitons are confined by the organic layers, improving radiative recombination efficiency [138]. It is well known that optimizing radiative recombination is desirable to achieve higher efficiency in LEDs, while the nonradiative recombination should be suppressed as much as possible, which requires the optimisation of the defect density, carrier mobility and exciton binding energy [131]. More breakthroughs in two-dimensional PeLEDs should be the defect-free film techniques and crystallization with various organic cations [183]. Ban et al. introduced a crown molecule to accurately control the phase separation and improve the quality of thin films [184]. As mentioned earlier, the film properties are better in 2D perovskites than those of 3D analogues. These extraordinary film-forming and exciton properties of 2D perovskites would produce remarkable enhancements of PLQE and EQE. In addition, although Mitzi (2001) indicated that pure 2D perovskites have even better film-forming properties than quasi-2D ones, the excitons in 2D perovskites could be quenched rapidly with nonradiative recombination, result in relatively low PL quantum yield [134]. As a result, the majority of impressive 2D perovskite LEDs with the outstanding performance are prepared with quasi-2D rather than pure 2D perovskites. In 1994, Era et al. fabricated LEDs using $(PEA)_2PbI_4$ perovskites with the structure of ITO/perovskite/OXD7/Mg/Ag [185]. They observed a strong EL peak at 520 nm at low temperature, and the brightness of the device was up to 10,000 cd/m^2 in maximum. Perovskites based light-emitting diodes have exceeded this value in terms of brightness [182]. The effective EL in early PeLED is originated from the introduction of OXD7, which acts as both a proper electron transport layer and a blocking layer to limit the holes pass through the light emitting layer [185]. Also, Yuan et al. suggested that the LEDs prepared with $PEA_2(CH_3NH_3)_4Pb_5I_{16}$ perovskites displayed a high EQE of around 8.8% in the near infrared region. When the perovskite film is 200 nm, the radiance could reach 80 W·m^2/sr [171]. This superior performance is due to the efficient accumulation and recombination of electrons and holes, which typically occurs in the lowest bandgap of the multiphase quasi-2D perovskites. Other more 2D perovskite LEDs reported in recent years and their specific performance parameters have been summarized in Table 2.

Table 2 2D/Quasi-2D perovskite-based LEDs and their performances

Perovskite emitter	EL (nm)	EQE_{max} (%)	CE_{max} (cd/A)	L_{max} (cd/m^2)	Refs.
$(PEA)_2PbI_4$	520	—	—	10,000	[185]
$(PEA)_2PbBr_4$	410	0.04	—	—	[138]
$(PEA)_2MA_4Pb_5I_{16}$	≈ 760	8.80	—	—	[171]
$(PEA)_2(MA)_{n-1}Pb_nBr_{3n+1}$	520	—	4.9	2,935	[170]
$(PEA)_2(FAPbBr_3)_{n-1}PbBr_4$	532	14.36	62.43	9,120	[178]
$(BA)_2(MA)_2Pb_3I_{10}$	700	2.29	0.10	214	[200]
$(BA)_2(MA)_4Pb_5Br_{16}$	523	1.01	3.48	2,246	[200]
$(BA)_2(MA)_2Pb_3Br_7Cl_3$	468	0.01	0.006	21	[200]
$(PEA)_2MA_4Pb_5Br_{16}$	526	7.4	—	8,400	[201]
$FAPbBr_3$	530	2.0	8.22	4,425	[202]
$(NMA)_2(FA)Pb_2I_7$	786	9.6	—	(55)[6]	[158]
$(NMA)_2(FA)Pb_2I_6Br$	763	11.7	—	(82)[6]	[158]
$BA_2MA_3Pb_4Br_{13}$	525	—	5.01	2,819	[203]
$CsPbCl_{0.9}Br_{2.1}$:PEABr	480	5.7	6.1	3,780	[188]

Furthermore, the 2D perovskites also contribute to achieving high colour rendering index (CRI) value of mixed-phosphor light sources. Mitzi (2004) stated that the highest CRI of 85 has been achieved using 2D perovskites in broadband single-source white-light emitters [186]. Recently reported green perovskites based LEDs have achieved a high EQE of 8.53% by decreasing the particle size of the perovskite-emitting layers. The PLQE was also increased to 36% at the same time [187], and the authors also stated that the colloidal perovskite nanoparticles with size smaller than 10 nm would show an extremely high PLQE even higher than 90%. So far, the impressive PLQE and EQE of 2D perovskite LED have been proved to be much higher than their 3D counterparts, especially in red and green colours [178]. A series of efficient red LEDs based on quasi-2D perovskite $(BA)_2Cs_{n-1}Pb_nI_{3n+1}$/PEO have been reported in 2018, where BA is benzyl ammonium and PEO is poly(ethylene oxide). The emission peaks are located at 638, 664, and 680 nm, respectively. The highest EQE of these devices reached to 6.23% at 680 nm and its brightness was about 1,293 cd/m^2. Also, it exhibited an exceptional EL spectral stability under repeated measurements [83]. In 2019, Li et al. also reported that the quantum efficiency of visible-light emitting perovskite LEDs has reached a milestone of 20 percent by managing the compositional distribution in the device, which also provides strong luminescence and effective charge injection [188]. More specifically, pre-synthesized $CsPbBr_3$ perovskites were firstly mixed with CH_3NH_3Br additive, whose different solubilities could sequentially generate crystallization into a $CsPbBr_3/CH_3NH_3Br$ quasi-core/shell structure. This shell could passivate the nonradiative defects in $CsPbBr_3$ crystals, promoting the PL quantum efficiency and enabling balanced charge injection. The EQE of 20.3% is a substantial step towards the practical application of perovskites based LEDs [188]. In terms of the blue 2D PeLEDs, although they have been reported, their performance remains moderate at current stage and there is great potential for improvement [138]. In 2019, Li et al. also reported that quasi-2D perovskites based LEDs with 480 nm blue emission have an EQE of 5.7%. Authors stated that the trap density of film surface was effectively reduced from around 4.1×10^{17} to 3.0×10^{16} cm^{-3} as the PEABr ratio increased from 0 to 100% by introducing PEABr into traditional 3D perovskite $CsPbCl_{0.9}Br_{2.1}$. Meanwhile, the PLQY of LEDs was enhanced from 0.15% to maximum of 27% [188]. It is further proved that the effective inhibition of non-radiative combination

is essential to the perovskites PL efficiency. Although great progress has been made in the 2D and quasi 2D perovskites-based LEDs, there are few drawbacks of those LEDs that need to be solved. For example, the charge transport in 2D or MQW perovskite LEDs are less efficient than 3D perovskites, which limits the improvement of power conversion efficiency. Maotao Yu et al. recently proposed a molecular engineering method to increase the conductivity of MQW perovskite films by reducing the barrier width in QWs, resulting in a peak external quantum efficiency of 7.7% [189]. In addition, the efficiency roll-off issue has also been observed in 2D layered perovskite LEDs. Wei Zou et al. recently reported that the efficiency roll-off in perovskite LEDs is mainly due to luminescence quenching which is likely caused by non-radiative Auger recombination [190]. This drawback can be suppressed by tuning the ratio of large and small organic cations in the precursor solution, leading to the optimized perovskite LEDs with external quantum efficiency of 12.7%.

From the review of 2D and 3D perovskite LEDs, it could be clearly seen that the EQE of 2D perovskite LEDs have developed rapidly in recent years for green and near-infrared emission. The current performance of 2D perovskite LEDs has been already approached to or even better than that of 3D organic-inorganic perovskite LEDs. Those achievements further consolidate the promise of 2D perovskites in light emitting applications.

4 Outlook and perspectives

Interest in 2D materials-based optoelectronics applications is growing dramatically across the scientific community owing to their extraordinary electrical and optical properties. In this review, we first overviewed the recent progress on TMDs preparation, their optical properties, and their light emitting applications. What should be noted is that the evolution of 2D materials LED started from simple single layer structure and then enriched to multiple layer stacking. The total conversion efficiency has increased from 0.01% to ~ 10%. The single layer lateral p-n junction structure can be tuned into devices with multiple functionalities by changing the bottom splitting gate voltage. However, the current injected efficiency further limited its application. To overcome this problem, the contact resistance must be reduced. Therefore, the surface modification and working function matching are essential in this particular structure. For the vertical stacking structure, this geometry has removed the back gates, thus reducing the power consumption. However, because of the ultra-thin nature of 2D stackings, there is always a very high current leakage. The h-BN layers must be employed in order to confine the injected carriers within the 2D optical active layers. With the development of the larger area 2D material CVD growth, especially for h-BN and TMDs, this stacking structure will exhibit tremendous potential for larger area on-chip light source applications with comparable energy conversion efficiency, and it may become an alternative option for commercial powder-based LED devices. In addition to above DC driven LED devices, the concept of AC driven LED is another research direction. Although it is still at its early stage, it has already presented advantages, including the simple design and pulsed features. Currently, the TMDs based high efficiency AC driven LEDs are mainly based on monolayer WS_2 due to its inherently high quantum yield. To extend this technology towards other type of TMDs, increasing optical quantum yield of those materials is still required. Light emitting application in TMDs is a continuing hot topic in this field. The research focus of next stage could be increasing the efficiency, exploring infrared LED based on novel materials such as BP LEDs. Combining materials synthesis and device designing, it could offer unprecedented opportunities for the future TMDs based on-chip optoelectronics applications.

Following the review of TMDs based light emitting applications, we critically reviewed the recent advances of 2D perovskite light emitting applications, including the materials synthesis, optical properties, and their light emitting devices. The excellent performance of 2D perovskites, such as the high crystallinity, high quantum yields, high exciton binding energies, narrow emission, and color tunability, making them particularly suitable for light emitting devices. Recently, Lin et al. have reported the high EQE (exceeds 20%) of quasi-core/shell structure perovskite organic light-emitting diodes (OLEDs), which is approaching to those of the best performance OLEDs [191]. With reported high efficiency perovskite LEDs, we believe that there is much room for improving the efficiency of perovskite LEDs owing to their great optoelectronic properties. In order to further improve the performance of perovskite LEDs, some strategies can be employed in this field. All available 2D perovskite materials at present are polycrystalline with randomly orientations, which usually causes insufficient charge transport compared to their single crystal counterparts. The poor charge transport will lead to limited performance of LEDs. Therefore, the single crystalline perovskite films are supposed to have lower defect density, better carrier mobility and better stability than conventional 2D perovskites. The single crystal perovskites hold great potential to fabricate ultra-high efficiency perovskite LEDs. However, synthesis of single crystal 2D perovskite remains a big challenge. More efforts should be devoted into this field. In addition, perovskite LEDs usually adopt multiple layered device structures with electron transport layer (ETL)/perovskite/hole transport layer (HTL). Those structure will cause serious PL quenching at the interface between perovskite and ETL (HTL) in perovskite LEDs, which will significantly affect the efficiency in LEDs. Therefore, the new structure designs or the perovskite surface passivation should be developed for tailoring to perovskite LEDs. Moreover, most of light generated from the perovskite emitter can be trapped within device, leading to low electroluminescence of LEDs. Therefore, the light outcoupling strategies should also be developed to further increase LEDs efficiency. For example, the specially designed substrate (double distribute reflector) and the use of micro lenses are typically solutions.

References

[1] Novoselov, K. S.; Jiang, D.; Schedin, F.; Booth, T. J.; Khotkevich, V. V.; Morozov, S. V.; Geim, A. K. Two-dimensional atomic crystals. *Proc. Natl. Acad. Sci. USA* **2005**, *102*, 10451–10453.

[2] Xu, M. S.; Liang, T.; Shi, M. M.; Chen, H. Z. Graphene-like two-dimensional materials. *Chem. Rev.* **2013**, *113*, 3766–3798.

[3] Nicolosi, V.; Chhowalla, M.; Kanatzidis, M. G.; Strano, M. S.; Coleman, J. N. Liquid exfoliation of layered materials. *Science* **2013**, *340*, 1226419.

[4] Radisavljevic, B.; Radenovic, A.; Brivio, J.; Giacometti, V.; Kis, A. Single-layer MoS_2 transistors. *Nat. Nanotechnol.* **2011**, *6*, 147–150.

[5] Splendiani, A.; Sun, L.; Zhang, Y. B.; Li, T. S.; Kim, J.; Chim, C. Y.; Galli, G.; Wang, F. Emerging photoluminescence in monolayer MoS_2. *Nano Lett.* **2010**, *10*, 1271–1275.

[6] Castellanos-Gomez, A.; van Leeuwen, R.; Buscema, M.; van der Zant, H. S. J.; Steele, G. A.; Venstra, W. J. Single-layer MoS_2 mechanical resonators. *Adv. Mater.* **2013**, *25*, 6719–6723.

[7] Lloyd, D.; Liu, X. H.; Boddeti, N.; Cantley, L.; Long, R.; Dunn, M. L.; Bunch, J. S. Adhesion, stiffness, and instability in atomically thin MoS_2 bubbles. *Nano Lett.* **2017**, *17*, 5329–5334.

[8] Gutiérrez, H. R.; Perea-López, N.; Elías, A. L.; Berkdemir, A.; Wang, B.; Lv, R. T.; López-Urías, F.; Crespi, V. H.; Terrones, H.; Terrones, M. Extraordinary room-temperature photoluminescence in triangular WS_2 monolayers. *Nano Lett*. **2013**, *13*, 3447–3454.

[9] Wu, W. Z.; Wang, L.; Li, Y. L.; Zhang, F.; Lin, K.; Niu, S. M.; Chenet, D.; Zhang, X.; Hao, Y. F.; Heinz, T. F. et al. Piezoelectricity of single-atomic-layer MoS_2 for energy conversion and piezotronics. *Nature* **2014**, *514*, 470–474.

[10] Sharma, A.; Zhang, L. L.; Tollerud, J. O.; Dong, M. H.; Zhu, Y.; Halbich, R.; Vogl, T.; Liang, K.; Nguyen, H T.; Wang, F. et al. Super-transport of excitons in atomically thin organic semiconductors at the 2D quantum limit. 2020, arXiv:2002.02623, 2020. arXiv.org e-Print archive. https://arxiv.org/abs/2002.02623 (accessed Mar 22, 2020).

[11] Khan, A. R.; Lu, T.; Ma, W. D.; Lu, Y. R.; Liu, Y. Tunable optoelectronic properties of WS_2 by local strain engineering and folding. *Adv. Electron. Mater*. **2020**, *6*, 1901381.

[12] Neupane, G. P.; Ma, W. D.; Yildirim, T.; Tang, Y. L.; Zhang, L. L.; Lu, Y. R. 2D organic semiconductors, the future of green nanotechnology. *Nano Mater. Sci*. **2019**, *1*, 246–259.

[13] Sharma, A.; Khan, A.; Zhu, Y.; Halbich, R.; Ma, W. D.; Tang, Y. L.; Wang, B. W.; Lu, Y. R. Quasi-line spectral emissions from highly crystalline one-dimensional organic nanowires. *Nano Lett*. **2019**, *19*, 7877–7886.

[14] Zhang, L. L.; Sharma, A.; Zhu, Y.; Zhang, Y. H.; Wang, B. W.; Dong, M. H.; Nguyen, H. T.; Wang, Z.; Wen, B.; Cao, Y. J. et al. Efficient and layer-dependent exciton pumping across atomically thin organic-inorganic type-I heterostructures. *Adv. Mater*. **2018**, *30*, 1803986.

[15] Sun, Z. P.; Martinez, A.; Wang, F. Optical modulators with 2D layered materials. *Nat. Photonics* **2016**, *10*, 227–238.

[16] Lu, J. P.; Yang, J.; Carvalho, A.; Liu, H, W.; Lu, Y. R.; Sow, C. H. Light–matter interactions in phosphorene. *Acc. Chem. Res*. **2016**, *49*, 1806–1815.

[17] Yang, J.; Xu, R. J.; Pei, J. J.; Myint, Y. W.; Wang, F.; Wang, Z.; Zhang, S.; Yu, Z. F.; Lu, Y. R. Optical tuning of exciton and trion emissions in monolayer phosphorene. *Light Sci. Appl*. **2015**, *4*, e312.

[18] Zhang, S.; Yang, J.; Xu, R. J.; Wang, F.; Li, W. F.; Ghufran, M.; Zhang, Y. W.; Yu, Z. F.; Zhang, G.; Qin, Q. H. et al. Extraordinary photoluminescence and strong temperature/angle-dependent Raman responses in few-layer phosphorene. *ACS Nano* **2014**, *8*, 9590–9596.

[19] Mak, K. F.; Shan, J. Photonics and optoelectronics of 2D semiconductor transition metal dichalcogenides. *Nat. Photonics* **2016**, *10*, 216–226.

[20] Wang, Q. H.; Kalantar-Zadeh, K.; Kis, A.; Coleman, J. N.; Strano, M. S. Electronics and optoelectronics of two-dimensional transition metal dichalcogenides. *Nat. Nanotechnol*. **2012**, *7*, 699–712.

[21] Carvalho, A.; Wang, M.; Zhu, X.; Rodin, A. S.; Su, H. B.; Castro Neto, A. H. Phosphorene: From theory to applications. *Nat. Rev. Mater*. **2016**, *1*, 16061.

[22] Mak, K. F.; Lee, C.; Hone, J.; Shan, J.; Heinz, T. F. Atomically thin MoS_2: A new direct-gap semiconductor. *Phys. Rev. Lett*. **2010**, *105*, 136805.

[23] Zhao, W. J.; Ribeiro, R. M.; Toh, M.; Carvalho, A.; Kloc, C.; Castro Neto, A. H.; Eda, G. Origin of indirect optical transitions in few-layer MoS_2, WS_2, and WSe_2. *Nano Lett*. **2013**, *13*, 5627–5634.

[24] Steinhoff, A.; Kim, J. H.; Jahnke, F.; Rösner, M.; Kim, D. S.; Lee, C.; Han, G. H.; Jeong, M. S.; Wehling, T. O.; Gies, C. Efficient excitonic photoluminescence in direct and indirect band gap monolayer MoS_2. *Nano Lett*. **2015**, *15*, 6841–6847.

[25] He, K. L.; Kumar, N.; Zhao, L.; Wang, Z. F.; Mak, K. F.; Zhao, H.; Shan, J. Tightly bound excitons in monolayer WSe_2. *Phys. Rev. Lett*. **2014**, *113*, 026803.

[26] Mak, K. F.; He, K. L, Lee, C.; Lee, G. H.; Hone, J.; Heinz, T. F.; Shan, J. Tightly bound trions in monolayer MoS_2. *Nat. Mater*. **2013**, *12*, 207–211.

[27] Moody, G.; Dass, C. K.; Hao, K.; Chen, C. H.; Li, L. J.; Singh, A.; Tran, K.; Clark, G.; Xu, X. D.; Berghäuser, G. et al. Intrinsic homogeneous linewidth and broadening mechanisms of excitons in monolayer transition metal dichalcogenides. *Nat. Commun*. **2015**, *6*, 8315.

[28] Ye, Z. L.; Cao, T.; O'Brien, K.; Zhu, H. Y.; Yin, X. B.; Wang, Y.; Louie, S. G.; Zhang, X. Probing excitonic dark states in single-layer tungsten disulphide. *Nature* **2014**, *513*, 214–218.

[29] Pei, J. J.; Yang, J.; Lu, Y. R. Elastic and inelastic light–matter interactions in 2D materials. *IEEE J. Sel. Top. Quantum Electron*. **2017**, *23*, 9000208.

[30] Pei, J. J.; Yang, J.; Yildirim, T.; Zhang, H.; Lu, Y. R. Many-body complexes in 2D semiconductors. *Adv. Mater*. **2019**, *31*, 1706945.

[31] Wang, X. M.; Xia, F. N. Van der Waals heterostructures: Stacked 2D materials shed light. *Nat. Mater*. **2015**, *14*, 264–265.

[32] Sharma, A.; Yan, H, Zhang, L. L.; Sun, X. Q.; Liu, B. Q.; Lu, Y. R. Highly enhanced many-body interactions in anisotropic 2D semiconductors. *Acc. Chem. Res*. **2018**, *51*, 1164–1173.

[33] Chen, H. T.; Corboliou, V.; Solntsev, A. S.; Choi, D. Y.; Vincenti, M. A.; de Ceglia, D.; de Angelis, C.; Lu, Y. R.; Neshev, D. N. Enhanced second-harmonic generation from two-dimensional $MoSe_2$ on a silicon waveguide. *Light Sci. Appl*. **2017**, *6*, e17060.

[34] Li, Y. L.; Rao, Y.; Mak, K. F.; You, Y. M.; Wang, S. Y.; Dean, C. R.; Heinz, T. F. Probing symmetry properties of few-layer MoS_2 and h-BN by optical second-harmonic generation. *Nano Lett*. **2013**, *13*, 3329–3333.

[35] Zhou, X. Cheng, J. X.; Zhou, Y. B.; Cao, T.; Hong, H.; Liao, Z. M.; Wu, S. W.; Peng, H. L.; Liu, K. H.; Yu, D. P. Strong second-harmonic generation in atomic layered GaSe. *J. Am. Chem. Soc*. **2015**, *137*, 7994–7997.

[36] Mennel, L.; Paur, M.; Mueller, T. Second harmonic generation in strained transition metal dichalcogenide monolayers: MoS_2, $MoSe_2$, WS_2, and WSe_2. *APL Photonics* **2019**, *4*, 034404.

[37] Chhowalla, M.; Liu, Z. F.; Zhang, H. Two-dimensional transition metal dichalcogenide (TMD) nanosheets. *Chem. Soc. Rev*. **2015**, *44*, 2584–2586.

[38] Schaibley, J. R.; Yu, H. Y.; Clark, G.; Rivera, P.; Ross, J. S.; Seyler, K. L.; Yao, W.; Xu, X. D. Valleytronics in 2D materials. *Nat. Rev. Mater*. **2016**, *1*, 16055.

[39] Qiu, D. Y.; da Jornada, F. H.; Louie, S. G. Screening and many-body effects in two-dimensional crystals: Monolayer MoS_2. *Phys. Rev. B* **2016**, *93*, 235435.

[40] You, Y. M.; Zhang, X. X.; Berkelbach, T. C.; Hybertsen, M. S.; Reichman, D. R.; Heinz, T. F. Observation of biexcitons in monolayer WSe_2. *Nat. Phys*. **2015**, *11*, 477–481.

[41] Wang, Z. F.; Rhodes, D. A., Watanabe, K.; Taniguchi, T.; Hone, J. C.; Shan, J.; Mak, K. F. Evidence of high-temperature exciton condensation in two-dimensional atomic double layers. *Nature* **2019**, *574*, 76–80.

[42] Rivera, P.; Yu, H. Y.; Seyler, K. L.; Wilson, N. P.; Yao, W.; Xu, X. D. Interlayer valley excitons in heterobilayers of transition metal dichalcogenides. *Nat. Nanotechnol*. **2018**, *13*, 1004–1015.

[43] Unuchek, D.; Ciarrocchi, A.; Avsar, A.; Watanabe, K.; Taniguchi, T.; Kis, A. Room-temperature electrical control of exciton flux in a van der Waals heterostructure. *Nature* **2018**, *560*, 340–344.

[44] Fogler, M. M.; Butov, L. V.; Novoselov, K. S. High-temperature superfluidity with indirect excitons in van der Waals heterostructures. *Nat. Commun*. **2014**, *5*, 4555.

[45] Barbone, M.; Montblanch, A. R.P.; Kara, D. M.; Palacios-Berraquero, C.; Cadore, A. R.; De Fazio, D.; Pingault, B.; Mostaani, E.; Li, H.; Chen, B. et al. Charge-tuneable biexciton complexes in monolayer WSe_2. *Nat. Commun*. **2018**, *9*, 3721.

[46] Han, K.; Ahn, G. H.; Cho, J.; Lien, D. H.; Amani, M.; Desai, S. B.; Zhang, G.; Kim, H.; Gupta, N.; Javey, A. et al. Bright electroluminescence in ambient conditions from WSe_2 p-n diodes using pulsed injection. *Appl. Phys. Lett*. **2019**, *115*, 011103.

[47] Lan, C. Y.; Zhou, Z. Y.; Wei, R. J.; Ho, J. C. Two-dimensional perovskite materials: From synthesis to energy-related applications. *Mater. Today Energy* **2019**, *11*, 61–82.

[48] Dou, L. T.; Wong, A. B.; Yu, Y.; Lai, M. L.; Kornienko, N.; Eaton, S. W.; Fu, A.; Bischak, C. G.; Ma, J.; Ding, T. N. et al. Atomically thin two-dimensional organic-inorganic hybrid perovskites. *Science* **2015**, *349*, 1518–1521.

[49] Blancon, J. C.; Tsai, H.; Nie, W.; Stoumpos, C. C.; Pedesseau, L.; Katan, C.; Kepenekian, M.; Soe, C. M. M.; Appavoo, K.; Sfeir, M. Y. et al. Extremely efficient internal exciton dissociation through edge states in layered 2D perovskites. *Science* **2017**, *355*, 1288–1292.

[50] Huo, C. X.; Cai, B.; Yuan, Z.; Ma, B. W.; Zeng, H. B. Two-dimensional metal halide perovskites: Theory, synthesis, and optoelectronics. *Small Methods* **2017**, *1*, 1600018.

[51] Tsai, H.; Nie, W. Y.; Blancon, J. C.; Stoumpos, C. C.; Asadpour, R.; Harutyunyan, B.; Neukirch, A. J.; Verduzco, R.; Crochet, J. J.; Tretiak, S. et al. High-efficiency two-dimensional ruddlesden-popper perovskite solar cells. *Nature* **2016**, *536*, 312–316.

[52] Farmer, D. B.; Golizadeh-Mojarad, R.; Perebeinos, V.; Lin, Y. M.; Tulevski, G. S.; Tsang, J. C.; Avouris, P. Chemical doping and electron–hole conduction asymmetry in graphene devices. *Nano Lett*. **2009**, *9*, 388–392.

[53] Peters, E. C.; Lee, E. J. H.; Burghard, M.; Kern, K. Gate dependent photocurrents at a graphene p-n junction. *Appl. Phys. Lett*. **2010**, *97*, 193102.

[54] Lemme, M. C.; Koppens, F. H. L.; Falk, A. L.; Rudner, M. S.; Park, H.; Levitov, L. S.; Marcus, C. M. Gate-activated photoresponse in a graphene p–n junction. *Nano Lett*. **2011**, *11*, 4134–4137.

[55] Baugher, B. W. H.; Churchill, H. O. H.; Yang, Y. F.; Jarillo-Herrero, P. Optoelectronic devices based on electrically tunable p–n diodes in a monolayer dichalcogenide. *Nat. Nanotechnol*. **2014**, *9*, 262–267.

[56] Lee, C. H.; Lee, G. H.; van der Zande, A. M.; Chen, W. C.; Li, Y. L.; Han, M. Y.; Cui, X.; Arefe, G.; Nuckolls, C.; Heinz, T. F. et al. Atomically thin p–n junctions with van der Waals heterointerfaces. *Nat. Nanotechnol*. **2014**, *9*, 676–681.

[57] Palacios-Berraquero, C.; Barbone, M.; Kara, D. M.; Chen, X. L.; Goykhman, I.; Yoon, D.; Ott, A. K.; Beitner, J.; Watanabe, K.; Taniguchi, T. et al. Atomically thin quantum light-emitting diodes. *Nat. Commun*. **2016**, *7*, 12978.

[58] Kang, J.; Tongay, S.; Zhou, J.; Li, J. B.; Wu, J. Q. Band offsets and heterostructures of two-dimensional semiconductors. *Appl. Phys. Lett*. **2013**, *102*, 012111.

[59] Moody, G.; Schaibley, J.; Xu, X. D. Exciton dynamics in monolayer transition metal dichalcogenides. *J. Opt. Soc. Am. B* **2016**, *33*, C39–C49.

[60] Jakubczyk, T.; Delmonte, V.; Koperski, M.; Nogajewski, K.; Faugeras, C.; Langbein, W.; Potemski, M.; Kasprzak, J. Radiatively limited dephasing and exciton dynamics in $MoSe_2$ monolayers revealed with four-wave mixing microscopy. *Nano Lett*. **2016**, *16*, 5333–5339.

[61] Mouri, S.; Miyauchi, Y.; Matsuda, K. Tunable photoluminescence of monolayer MoS_2 via chemical doping. *Nano Lett*. **2013**, *13*, 5944–5948.

[62] Ross, J. S.; Wu, S. F.; Yu, H. Y.; Ghimire, N. J.; Jones, A. M.; Aivazian, G.; Yan, J. Q.; Mandrus, D. G.; Xiao, D.; Yao, W. et al. Electrical control of neutral and charged excitons in a monolayer semiconductor. *Nat. Commun*. **2013**, *4*, 1474.

[63] Yang, J.; Lü, T. Y.; Myint, Y. W.; Pei, J. J.; Macdonald, D.; Zheng, J. C.; Lu, Y. R. Robust excitons and trions in monolayer $MoTe_2$. *ACS Nano* **2015**, *9*, 6603–6609.

[64] Amani, M.; Lien, D. H.; Kiriya, D.; Xiao, J.; Azcatl, A.; Noh, J.; Madhvapathy, S. R.; Addou, R.; KC, S.; Dubey, M. et al. Near-unity photoluminescence quantum yield in MoS_2. *Science* **2015**, *350*, 1065–1068.

[65] Voiry, D.; Mohite, A.; Chhowalla, M. Phase engineering of transition metal dichalcogenides. *Chem. Soc. Rev*. **2015**, *44*, 2702–2712.

[66] Tan, C. L.; Cao, X. H.; Wu, X. J.; He, Q. Y.; Yang, J.; Zhang, X.; Chen, J. Z.; Zhao, W.; Han, S. K.; Nam, G. H. et al. Recent advances in ultrathin two-dimensional nanomaterials. *Chem. Rev*. **2017**, *117*, 6225–6331.

[67] Castellanos-Gomez, A.; Buscema, M.; Molenaar, R.; Singh, V.; Janssen, L.; van der Zant, H. S. J.; Steele, G. A. Deterministic transfer of two-dimensional materials by all-dry viscoelastic stamping. *2D Mater*. **2014**, *1*, 011002.

[68] Novoselov, K. S.; Geim, A. K.; Morozov, S. V.; Jiang, D.; Katsnelson, M. I.; Grigorieva, I. V.; Dubonos, S. V.; Firsov, A. A. Two-dimensional gas of massless Dirac fermions in graphene. *Nature* **2005**, *438*, 197–200.

[69] Wen, B.; Zhu, Y.; Yudistira, D.; Boes, A.; Zhang, L. L.; Yidirim, T.; Liu, B. Q.; Yan, H.; Sun, X. Q.; Zhou, Y. et al. Ferroelectric-driven exciton and trion modulation in monolayer molybdenum and tungsten diselenides. *ACS Nano* **2019**, *13*, 5335–5343.

[70] Coleman, J. N.; Lotya, M.; O'Neill, A.; Bergin, S. D.; King, P. J.; Khan, U.; Young, K.; Gaucher, A.; De, S.; Smith, R. J. et al. Two-dimensional nanosheets produced by liquid exfoliation of layered materials. *Science* **2011**, *331*, 568–571.

[71] Yasaei, P.; Kumar, B.; Foroozan, T.; Wang, C. H.; Asadi, M.; Tuschel, D.; Indacochea, J. E.; Klie, R. F.; Salehi-Khojin, A. High-quality black phosphorus atomic layers by liquid-phase exfoliation. *Adv. Mater*. **2015**, *27*, 1887–1892.

[72] Zeng, Z. Y.; Yin, Z. Y.; Huang, X.; Li, H.; He, Q. Y.; Lu, G.; Boey, F.; Zhang, H. Single-layer semiconducting nanosheets: High-yield preparation and device fabrication. *Angew. Chem*. **2011**, *123*, 11289–11293.

[73] Fan, X. B.; Xu, P. T.; Zhou, D. K.; Sun, Y. F.; Li, Y. G.; C.; Nguyen, M. A. T.; Terrones, M.; Mallouk, T. E. Fast and efficient preparation of exfoliated 2H MoS_2 nanosheets by sonication-assisted lithium intercalation and infrared laser-induced 1T to 2H phase reversion. *Nano Lett*. **2015**, *15*, 5956–5960.

[74] Pei, J. J.; Yang, J.; Wang, X. B.; Yu, Z. F.; Choi, D. Y.; Luther-Davies, B.; Lu, Y. R. Producing air-stable monolayers of phosphorene and their defect engineering. *Nat. Commun*. **2016**, *7*, 10450.

[75] Vogl, T.; Lu, Y. R.; Lam, P. K. Room temperature single photon source using fiber-integrated hexagonal boron nitride. *J. Phys. D Appl. Phys*. **2017**, *50*, 295101.

[76] Zeng, Z. Y.; Sun, T.; Zhu, J. X.; Huang, Xiao.; Yin, Z. Y.; Lu, G.; Fan, Z. X.; Yan, Q. Y.; Hng, H. H.; Zhang, H. An effective method for the fabrication of few-layer-thick inorganic nanosheets. *Angew. Chem., Int. Ed*. **2012**, *51*, 9052–9056.

[77] Huang, Y.; Pan, Y. H.; Yang, R.; Bao, L. H.; Meng, L.; Luo, H. L.; Cai, Y. Q.; Liu, G. D.; Zhao, W. J.; Zhou, Z. et al. Universal mechanical exfoliation of large-area 2D crystals. *Nat. Commun*. **2020**, *11*, 2453.

[78] Liu, K. K.; Zhang, W. J.; Lee, Y. H.; Lin, Y. C.; Chang, M. T.; Su, C. Y.; Chang, C. S.; Li, H.; Shi, Y. M.; Zhang, H. et al. Growth of large-area and highly crystalline MoS_2 thin layers on insulating substrates. *Nano Lett*. **2012**, *12*, 1538–1544.

[79] Zhu, Y.; Yang, J.; Zhang, S.; Mokhtar, S.; Pei, J. J.; Wang, X. H.; Lu, Y. R. Strongly enhanced photoluminescence in nanostructured monolayer MoS_2 by chemical vapor deposition. *Nanotechnology* **2016**, *27*, 135706.

[80] Wang, X. L.; Gong, Y. J.; Shi, G.; Chow, W. L.; Keyshar, K.; Ye, G. L.; Vajtai, R.; Lou, J.; Liu, Z.; Ringe, E. et al. Chemical vapor deposition growth of crystalline monolayer $MoSe_2$. *ACS Nano* **2014**, *8*, 5125–5131.

[81] Chen, P.; Zhang, Z. W.; Duan, X. D.; Duan, X. F. Chemical synthesis of two-dimensional atomic crystals, heterostructures and superlattices. *Chem. Soc. Rev*. **2018**, *47*, 3129–3151.

[82] Kang, K.; Xie, S. E.; Huang, L. J.; Han, Y. M.; Huang, P. Y.; Mak, K. F.; Kim, C. J.; Muller, D.; Park, J. High-mobility three-atom-thick semiconducting films with wafer-scale homogeneity. *Nature* **2015**, *520*, 656–660.

[83] Tian, Y.; Zhou, C. K.; Worku, M.; Wang, X.; Ling, Y. C.; Gao, H. W.; Zhou, Y.; Miao, Y.; Guan, J. J.; Ma, B. W. Highly efficient spectrally stable red perovskite light-emitting diodes. *Adv. Mater*. **2018**, *30*, 1707093.

[84] Miller, R. C.; Kleinman, D. A.; Tsang, W. T.; Gossard, A. C. Observation of the excited level of excitons in GaAs quantum wells. *Phys. Rev. B* **1981**, *24*, 1134–1136.

[85] Miller, R. C.; Kleinman, D. A. Excitons in GaAs quantum wells. *J. Lumin*. **1985**, *30*, 520–540.

[86] Chernikov, A.; Berkelbach, T. C.; Hill, H. M.; Rigosi, A.; Li, Y. L.; Aslan, O. B.; Reichman, D. R.; Hybertsen, M. S.; Heinz, T. F. Exciton binding energy and nonhydrogenic Rydberg series in monolayer WS_2. *Phys. Rev. Lett*. **2014**, *113*, 076802.

[87] Cheiwchanchamnangij, T.; Lambrecht, W. R. L. Quasiparticle band structure calculation of monolayer, bilayer, and bulk MoS_2. *Phys. Rev. B* **2012**, *85*, 205302.

[88] Ramasubramaniam, A. Large excitonic effects in monolayers of molybdenum and tungsten dichalcogenides. *Phys. Rev. B* **2012**, *86*, 115409.

[89] Park, S.; Mutz, N.; Schultz, T.; Blumstengel, S.; Han, A.; Aljarb, A.; Li, L. J.; List-Kratochvil, E. J. W.; Amsalem, P.; Koch, N. Direct determination of monolayer MoS_2 and WSe_2 exciton binding energies on insulating and metallic substrates. *2D Mater*. **2018**, *5*, 025003.

[90] Zhu, B. R.; Chen, X.; Cui, X. D. Exciton binding energy of monolayer WS_2. *Sci. Rep*. **2015**, *5*, 9218.

[91] Ugeda, M. M.; Bradley, A. J.; Shi, S. F.; da Jornada, F. H.; Zhang, Y.; Qiu, D. Y.; Ruan, W.; Mo, S. K.; Hussain, Z.; Shen, Z. X. et al.

Giant bandgap renormalization and excitonic effects in a monolayer transition metal dichalcogenide semiconductor. *Nat. Mater.* **2014**, *13*, 1091–1095.

[92] Kübler, J. K. The exciton binding energy of III–V semiconductor compounds. *Phys. Status Solidi B* **1969**, *35*, 189–195.

[93] Hao, K.; Specht, J. F.; Nagler, P.; Xu, L. X.; Tran, K.; Singh, A.; Dass, C. K.; Schüller, C; Korn, T.; Richter, M. et al. Neutral and charged inter-valley biexcitons in monolayer $MoSe_2$. *Nat. Commun.* **2017**, *8*, 15552.

[94] Ross, J. S.; Klement, P.; Jones, A. M.; Ghimire, N. J.; Yan, J. Q.; Mandrus, D. G.; Taniguchi, T.; Watanabe, K.; Kitamura, K.; Yao, W. et al. Electrically tunable excitonic light-emitting diodes based on monolayer WSe_2 p–n junctions. *Nat. Nanotechnol.* **2014**, *9*, 268–272.

[95] Jo, S.; Ubrig, N.; Berger, H.; Kuzmenko, A. B.; Morpurgo, A. F. Mono- and bilayer WS_2 light-emitting transistors. *Nano Lett.* **2014**, *14*, 2019–2025.

[96] Zhang, Y. J.; Oka, T.; Suzuki, R.; Ye, J. T.; Iwasa, Y. Electrically switchable chiral light-emitting transistor. *Science* **2014**, *344*, 725–728.

[97] Cheng, R.; Li, D. H.; Zhou, H. L.; Wang, C.; Yin, A. X.; Jiang, S.; Liu, Y.; Chen, Y.; Huang, Y.; Duan, X. F. Electroluminescence and photocurrent generation from atomically sharp WSe_2/MoS_2 heterojunction p–n diodes. *Nano Lett.* **2014**, *14*, 5590–5597.

[98] Britnell, L.; Gorbachev, R. V.; Jalil, R.; Belle, B. D.; Schedin, F.; Katsnelson, M. I.; Eaves, L.; Morozov, S. V.; Mayorov, A. S.; Peres, N. M. R. et al. Electron tunneling through ultrathin boron nitride crystalline barriers. *Nano Lett.* **2012**, *12*, 1707–1710.

[99] Lee, G. H.; Yu, Y. J.; Lee, C.; Dean, C.; Shepard, K. L.; Kim, P.; Hone, J. Electron tunneling through atomically flat and ultrathin hexagonal boron nitride. *Appl. Phys. Lett.* **2011**, *99*, 243114.

[100] Withers, F.; Del Pozo-Zamudio, O.; Mishchenko, A.; Rooney, A. P.; Gholinia, A.; Watanabe, K.; Taniguchi, T.; Haigh, S. J.; Geim, A. K.; Tartakovskii, A. I. et al. Light-emitting diodes by band-structure engineering in van der Waals heterostructures. *Nat. Mater.* **2015**, *14*, 301–306.

[101] Withers, F.; Del Pozo-Zamudio, O.; Schwarz, S.; Dufferwiel, S.; Walker, P. M.; Godde, T.; Rooney, A. P.; Gholinia, A.; Woods, C. R.; Blake, P. et al. WSe_2 light-emitting tunneling transistors with enhanced brightness at room temperature. *Nano Lett.* **2015**, *15*, 8223–8228.

[102] Liu, C. H.; Clark, G.; Fryett, T.; Wu, S. F.; Zheng, J. J.; Hatami, F.; Xu, X. D.; Majumdar, A. Nanocavity integrated van der Waals heterostructure light-emitting tunneling diode. *Nano Lett.* **2017**, *17*, 200–205.

[103] Gorbachev, R. V.; Riaz, I.; Nair, R R.; Jalil, R.; Britnell, L.; Belle, B. D.; Hill, E. W.; Novoselov, K. S.; Watanabe, K.; Taniguchi, T. et al. Hunting for monolayer boron nitride: Optical and Raman signatures. *Small* **2011**, *7*, 465–468.

[104] Pyatkov, F.; Fütterling, V.; Khasminskaya, S.; Flavel, B. S.; Hennrich, F.; Kappes, M. M.; Krupke, R.; Pernice, W. H. P. Cavity-enhanced light emission from electrically driven carbon nanotubes. *Nat. Photonics* **2016**, *10*, 420.

[105] Birowosuto, M. D.; Yokoo, A.; Zhang, G. Q.; Tateno, K.; Kuramochi, E.; Taniyama, H.; Takiguchi, M.; Notomi, M. Movable high-*Q* nanoresonators realized by semiconductor nanowires on a Si photonic crystal platform. *Nat. Mater.* **2014**, *13*, 279–285.

[106] Wang, H.; Yu, L. L.; Lee, Y. H.; Shi, Y. M.; Hsu, A.; Chin, M. L.; Li, L. J.; Dubey, M.; Kong, J.; Palacios, T. Integrated circuits based on bilayer MoS_2 transistors. *Nano Lett.* **2012**, *12*, 4674–4680.

[107] Radisavljevic, B.; Whitwick, M. B.; Kis, A. Integrated circuits and logic operations based on single-layer MoS_2. *ACS Nano* **2011**, *5*, 9934–9938.

[108] Ruppert, C.; Aslan, O. B.; Heinz, T. F. Optical properties and band gap of single-and few-layer $MoTe_2$ crystals. *Nano Lett.* **2014**, *14*, 6231–6236.

[109] Zhu, Y.; Li, Z. Y.; Zhang, L. L.; Wang, B. W.; Luo, Z. Q.; Long, J. Z.; Yang, J.; Fu, L.; Lu, Y. R. High-efficiency monolayer molybdenum ditelluride light-emitting diode and photodetector. *ACS Appl. Mater. Interfaces* **2018**, *10*, 43291–43298.

[110] Bie, Y. Q.; Grosso, G.; Heuck, M.; Furchi, M. M.; Cao, Y.; Zheng, J. B.; Bunandar, D.; Navarro-Moratalla, E.; Zhou, L.; Efetov, D. K. et al. A $MoTe_2$-based light-emitting diode and photodetector for silicon photonic integrated circuits. *Nat. Nanotechnol.* **2017**, *12*, 1124–1129.

[111] Xu, R. J.; Zhang, S.; Wang, F.; Yang, J.; Wang, Z.; Pei, J. J.; Myint, Y. W.; Xing, B. B.; Yu, Z. F.; Fu, L. et al. Extraordinarily bound quasi-one-dimensional trions in two-dimensional phosphorene atomic semiconductors. *ACS Nano* **2016**, *10*, 2046–2053.

[112] Xu, R. J.; Yang, J.; Myint, Y. W.; Pei, J. J.; Yan, H.; Wang, F.; Lu, Y. R. Exciton brightening in monolayer phosphorene via dimensionality modification. *Adv. Mater.* **2016**, *28*, 3493–3498.

[113] Wang, J. J.; Rousseau, A.; Yang, M.; Low, T.; Francoeur, S.; Kéna-Cohen, S. Mid-infrared polarized emission from black phosphorus light-emitting diodes. *Nano Lett.* **2020**, *20*, 3651–3655.

[114] Chen, C.; Chen, F.; Chen, X. L.; Deng, B. C.; Eng, B.; Jung, D.; Guo, Q. S.; Yuan, S. F.; Watanabe, K.; Taniguchi, T. et al. Bright mid-infrared photoluminescence from thin-film black phosphorus. *Nano Lett.* **2019**, *19*, 1488–1493.

[115] Li, L. K.; Yu, Y. J.; Ye, G. J.; Ge, Q. Q.; Ou, X. D.; Wu, H.; Feng, D. L.; Chen, X. H.; Zhang, Y. B. Black phosphorus field-effect transistors. *Nat. Nanotechnol.* **2014**, *9*, 372–377.

[116] Koenig, S. P.; Doganov, R. A.; Schmidt, H.; Castro Neto, A. H.; Özyilmaz, B. Electric field effect in ultrathin black phosphorus. *Appl. Phys. Lett.* **2014**, *104*, 103106.

[117] Liu, H.; Neal, A. T.; Zhu, Z.; Luo, Z.; Xu, X. F.; Tománek, D.; Ye, P. D. Phosphorene: An unexplored 2D semiconductor with a high hole mobility. *ACS Nano* **2014**, *8*, 4033–4041.

[118] Buscema, M.; Groenendijk, D. J.; Blanter, S. I.; Steele, G. A.; van der Zant, H. S. J.; Castellanos-Gomez, A. Fast and broadband photoresponse of few-layer black phosphorus field-effect transistors. *Nano Lett.* **2014**, *14*, 3347–3352.

[119] Xia, F. N.; Wang, H.; Jia, Y. C. Rediscovering black phosphorus as an anisotropic layered material for optoelectronics and electronics. *Nat. Commun.* **2014**, *5*, 4458.

[120] Politi, A.; Matthews, J. C. F.; O'Brien, J. L. Shor's quantum factoring algorithm on a photonic chip. *Science* **2009**, *325*, 1221.

[121] Koperski, M.; Nogajewski, K.; Arora, A.; Cherkez, V.; Mallet, P.; Veuillen, J. Y.; Marcus, J.; Kossacki, P.; Potemski, M. Single photon emitters in exfoliated WSe_2 structures. *Nat. Nanotechnol.* **2015**, *10*, 503–506.

[122] Yuan, Z. L.; Kardynal, B. E.; Stevenson, R. M.; Shields, A. J.; Lobo, C. J.; Cooper, K.; Beattie, N. S.; Ritchie, D. A.; Pepper, M. Electrically driven single-photon source. *Science* **2002**, *295*, 102–105.

[123] Clark, G.; Schaibley, J. R.; Ross, J.; Taniguchi, T.; Watanabe, K.; Hendrickson, J. R.; Mou, S.; Yao, W.; Xu, X. D. Single defect light-emitting diode in a van der Waals heterostructure. *Nano Lett.* **2016**, *16*, 3944–3948.

[124] Nakamura, S.; Senoh, M.; Mukai, T. High-power InGaN/GaN double-heterostructure violet light emitting diodes. *Appl. Phys. Lett.* **1993**, *62*, 2390–2392.

[125] Lien, D. H.; Amani, M.; Desai, S. B.; Ahn, G. H.; Han, K.; He, J. H.; Ager III, J. W.; Wu, M. C.; Javey, A. Large-area and bright pulsed electroluminescence in monolayer semiconductors. *Nat. Commun.* **2018**, *9*, 1229.

[126] Cho, J.; Amani, M.; Lien, D. H.; Kim, H.; Yeh, M.; Wang, V.; Tan, C. L.; Javey, A. Centimeter-scale and visible wavelength monolayer light-emitting devices. *Adv. Funct. Mater.* **2020**, *30*, 1907941.

[127] Paur, M.; Molina-Mendoza, A. J.; Bratschitsch, R.; Watanabe, K.; Taniguchi, T.; Mueller, T. Electroluminescence from multi-particle exciton complexes in transition metal dichalcogenide semiconductors. *Nat. Commun.* **2019**, *10*, 1709.

[128] Ma, S.; Cai, M. L.; Cheng, T.; Ding, X. H.; Shi, X. Q.; Alsaedi, A.; Hayat, T.; Ding, Y.; Tan, Z. A.; Dai, S. Y. Two-dimensional organic-inorganic hybrid perovskite: From material properties to device applications. *Sci. China Mater.* **2018**, *61*, 1257–1277.

[129] Loryuenyong, V.; Thongpon, P.; Saudmalai, S.; Buasri, A. The synthesis of 2D $CH_3NH_3PbI_3$ perovskite films with tunable bandgaps by solution deposition route. *Int. J. Photoener.* **2019**, *2019*, 7492453.

[130] Xue, Y. Z.; Yuan, J.; Liu, J. Y.; Li, S. J. Controllable synthesis of 2D perovskite on different substrates and its application as photodetector. *Nanomaterials* **2018**, *8*, 591.

[131] Gao, X. P.; Zhang, X. T.; Yin, W. X.; Wang, H.; Hu, Y.; Zhang, Q. B.; Shi, Z. F.; Colvin, V. L.; Yu, W. W.; Zhang, Y. Ruddlesden–Popper perovskites: Synthesis and optical properties for optoelectronic

applications. *Adv. Sci*. **2019**, *6*, 1900941.
[132] Zhang, L.; Liu, Y. C.; Yang, Z.; Liu, S. Z. Two dimensional metal halide perovskites: Promising candidates for light-emitting diodes. *J. Energy Chem*. **2019**, *37*, 97–110.
[133] Fang, C.; Li, J. Z.; Wang, J.; Chen, R.; Wang, H. Z.; Lan, S. G.; Xuan, Y. N.; Luo, H. M.; Fei, P.; Li, D. H. Controllable growth of two-dimensional perovskite microstructures. *CrystEngComm* **2018**, *20*, 6538–6545.
[134] Gauthron, K.; Lauret, J. S.; Doyennette, L.; Lanty, G.; Al Choueiry, A.; Zhang, S. J.; Brehier, A.; Largeau, L.; Mauguin, O.; Bloch, J. et al. Optical spectroscopy of two-dimensional layered $(C_6H_5C_2H_4\text{-}NH_3)_2\text{-}PbI_4$ perovskite. *Opt. Express* **2010**, *18*, 5912–5919.
[135] Gao, Y.; Shi, E. Z.; Deng, S. B.; Shiring, S. B.; Snaider, J. M.; Liang, C.; Yuan, B.; Song, R. Y.; Janke, S. M.; Liebman-Peláez, A. et al. Molecular engineering of organic–inorganic hybrid perovskites quantum wells. *Nat. Chem*. **2019**, *11*, 1151–1157.
[136] Quan, L. N.; Yuan, M. J.; Comin, R.; Voznyy, O.; Beauregard, E. M.; Hoogland, S.; Buin, A.; Kirmani, A. R.; Zhao, K.; Amassian, A. et al. Ligand-stabilized reduced-dimensionality perovskites. *J. Am. Chem. Soc*. **2016**, *138*, 2649–2655.
[137] Mercier, N.; Poiroux, S.; Riou, A.; Batail, P. Unique hydrogen bonding correlating with a reduced band gap and phase transition in the hybrid perovskites $(HO(CH_2)_2NH_3)_2PbX_4$ (X = I, Br). *Inorg. Chem*. **2004**, *43*, 8361–8366.
[138] Liang, D.; Peng, Y. L.; Fu, Y. P.; Shearer, M. J.; Zhang, J. J.; Zhai, J. Y.; Zhang, Y.; Hamers, R. J.; Andrew, T. L.; Jin, S. Color-pure violet-light-emitting diodes based on layered lead halide perovskite nanoplates. *ACS Nano* **2016**, *10*, 6897–6904.
[139] Jeon, N. J.; Noh, J. H.; Kim, Y. C.; Yang, W. S.; Ryu, S.; Seok, S. I. Solvent engineering for high-performance inorganic–organic hybrid perovskite solar cells. *Nat. Mater*. **2014**, *13*, 897–903.
[140] Bi, C.; Wang, Q.; Shao, Y. C.; Yuan, Y. B.; Xiao, Z. G.; Huang, J. S. Non-wetting surface-driven high-aspect-ratio crystalline grain growth for efficient hybrid perovskite solar cells. *Nat. Commun*. **2015**, *6*, 7747.
[141] Liu, J. Y.; Xue, Y. Z.; Wang, Z. Y.; Xu, Z. Q.; Zheng, C. X.; Weber, B.; Song, J. C.; Wang, Y. S.; Lu, Y. R.; Zhang, Y. P. et al. Two-dimensional $CH_3NH_3PbI_3$ perovskite: Synthesis and optoelectronic application. *ACS Nano* **2016**, *10*, 3536–3542.
[142] Zhang, Y. Z.; Chen, J. H.; Lian, X. M.; Qin, M. C.; Li, J.; Andersen, T. R.; Lu, X. H.; Wu, G.; Li, H. Y.; Chen, H. Z. Highly efficient guanidinium-based quasi 2D perovskite solar cells via a two-step post-treatment process. *Small Methods* **2019**, *3*, 1900375.
[143] Tavakoli, M. M.; Gu, L. L.; Gao, Y.; Reckmeier, C.; He, J.; Rogach, A. L.; Yao, Y.; Fan, Z. Y. Fabrication of efficient planar perovskite solar cells using a one-step chemical vapor deposition method. *Sci. Rep*. **2015**, *5*, 14083.
[144] Liu, M. Z.; Johnston, M. B.; Snaith, H. J. Efficient planar heterojunction perovskite solar cells by vapour deposition. *Nature* **2013**, *501*, 395–398.
[145] Ha, S. T.; Liu, X. F.; Zhang, Q.; Giovanni, D.; Sum, T. C.; Xiong, Q. H. Synthesis of organic-inorganic lead halide perovskite nanoplatelets: Towards high-performance perovskite solar cells and optoelectronic devices. *Adv. Opt. Mater*. **2014**, *2*, 838–844.
[146] Wang, Y. P.; Shi, Y. F.; Xin, G. Q.; Lian, J.; Shi, J. Two-dimensional van der Waals epitaxy kinetics in a three-dimensional perovskite halide. *Cryst. Growth Des*. **2015**, *15*, 4741–4749.
[147] Shi, E. Z.; Gao, Y.; Finkenauer, B. P.; Akriti; Coffey, A. H.; Dou, L. T. Two-dimensional halide perovskite nanomaterials and heterostructures. *Chem. Soc. Rev*. **2018**, *47*, 6046–6072.
[148] Leng, K.; Fu, W.; Liu, Y. P.; Chhowalla, M.; Loh, K. P. From bulk to molecularly thin hybrid perovskites. *Nat. Rev. Mater*. **2020**, *5*, 482–500.
[149] Koh, T. M.; Shanmugam, V.; Schlipf, J.; Oesinghaus, L.; Müller-Buschbaum, P.; Ramakrishnan, N.; Swamy, V.; Mathews, N.; Boix, P. P.; Mhaisalkar, S. G. Nanostructuring mixed-dimensional perovskites: A route toward tunable, efficient photovoltaics. *Adv. Mater*. **2016**, *28*, 3653–3661.
[150] Ishihara, T.; Takahashi, J.; Goto, T. Exciton state in two-dimensional perovskite semiconductor $(C_{10}H_{21}NH_3)_2PbI_4$. *Solid State Commun* **1989**, *69*, 933–936.
[151] Sichert, J. A.; Tong, Y.; Mutz, N.; Vollmer, M.; Fischer, S.; Milowska, K. Z.; García Cortadella, R.; Nickel, B.; Cardenas-Daw, C.; Stolarczyk, J. K. et al. Quantum size effect in organometal halide perovskite nanoplatelets. *Nano Lett*. **2015**, *15*, 6521–6527.
[152] Mao, L. L.; Stoumpos, C. C.; Kanatzidis, M. G. Two-dimensional hybrid halide perovskites: Principles and promises. *J. Am. Chem. Soc*. **2019**, *141*, 1171–1190.
[153] Guerra, V. L. P.; Kovaříček, P.; Valeš, V.; Drogowska, K.; Verhagen, T.; Vejpravova, J.; Horák, L.; Listorti, A.; Colella, S.; Kalbáč, M. Selective self-assembly and light emission tuning of layered hybrid perovskites on patterned graphene. *Nanoscale* **2018**, *10*, 3198–3211.
[154] Dohner, E. R.; Hoke, E. T.; Karunadasa, H. I. Self-assembly of broadband white-light emitters. *J. Am. Chem. Soc*. **2014**, *136*, 1718–1721.
[155] Manser, J. S.; Christians, J. A.; Kamat, P. V. Intriguing optoelectronic properties of metal halide perovskites. *Chem. Rev*. **2016**, *116*, 12956–13008.
[156] Sun, Y.; Zhang, L.; Wang, N. N.; Zhang, S. T.; Cao, Yu.; Miao, Y. F.; Xu, M. M.; Zhang, H.; Li, H.; Yi, C. et al. The formation of perovskite multiple quantum well structures for high performance light-emitting diodes. *npj Flex. Electron*. **2018**, *2*, 12.
[157] Zhang, S. T.; Yi, C.; Wang, N. N.; Sun, Y.; Zou, W.; Wei, Y. Q.; Cao, Y.; Miao, Y. F.; Li, R. Z.; Yin, Y. et al. Efficient red perovskite light-emitting diodes based on solution-processed multiple quantum Wells. *Adv. Mater*. **2017**, *29*, 1606600.
[158] Wang, N. N.; Cheng, L.; Ge, R.; Zhang, S. T.; Miao, Y. F.; Zou, W.; Yi, C.; Sun, Y.; Cao, Y.; Yang, R. et al. Perovskite light-emitting diodes based on solution-processed self-organized multiple quantum wells. *Nat. Photonics* **2016**, *10*, 699–704.
[159] Grancini, G.; Nazeeruddin, M. K. Dimensional tailoring of hybrid perovskites for photovoltaics. *Nat. Rev. Mater*. **2019**, *4*, 4–22.
[160] Stoumpos, C. C.; Cao, D. H.; Clark, D. J.; Young, J.; Rondinelli, J. M.; Jang, J. I.; Hupp, J. T.; Kanatzidis, M. G. Ruddlesden–Popper hybrid lead iodide perovskite 2D homologous semiconductors. *Chem. Mater*. **2016**, *28*, 2852–2867.
[161] Venkatesan, N. R.; Labram, J. G.; Chabinyc, M. L. Charge-carrier dynamics and crystalline texture of layered Ruddlesden–Popper hybrid lead iodide perovskite thin films. *ACS Energy Lett*. **2018**, *3*, 380–386.
[162] Chen, A. Z.; Shiu, M.; Ma, J. H.; Alpert, M. R.; Zhang, D. P.; Foley, B. J.; Smilgies, D. M.; Lee, S. H.; Choi, J. J. Origin of vertical orientation in two-dimensional metal halide perovskites and its effect on photovoltaic performance. *Nat. Commun*. **2018**, *9*, 1336.
[163] Hong, X.; Ishihara, T.; Nurmikko, A. V. Dielectric confinement effect on excitons in PbI_4-based layered semiconductors. *Phys. Rev. B* **1992**, *45*, 6961–6964.
[164] Kumagai, M.; Takagahara, T. Excitonic and nonlinear-optical properties of dielectric quantum-well structures. *Phys. Rev. B* **1989**, *40*, 12359.
[165] Dou, L. T. Emerging two-dimensional halide perovskite nanomaterials. *J. Mater. Chem. C* **2017**, *5*, 11165–11173.
[166] Kitazawa, N.; Watanabe, Y. Optical properties of natural quantum-well compounds $(C_6H_5\text{-}C_nH_{2n}\text{-}NH_3)_2PbBr_4$ (n = 1–4). *J. Phys. Chem. Solids* **2010**, *71*, 797–802.
[167] Mitzi, D. B.; Feild, C.; Harrison, W. T. A.; Guloy, A. M. Conducting tin halides with a layered organic-based perovskite structure. *Nature* **1994**, *369*, 467–469.
[168] Jones, E. D.; Drummond, T. J.; Hjalmarson, H. P.; Schirber, J. E. Photoluminescence studies of GaAs/AlAs short period superlattices. *Superlatt. Microstruct*. **1988**, *4*, 233–236.
[169] Yaffe, O.; Chernikov, A.; Norman, Z. M.; Zhong, Y.; Velauthapillai, A.; van der Zande, A.; Owen, J. S.; Heinz, T. F. Excitons in ultrathin organic-inorganic perovskite crystals. *Phys. Rev. B* **2015**, *92*, 045414.
[170] Byun, J.; Cho, H.; Wolf, C.; Jang, M.; Sadhanala, A.; Friend, R. H.; Yang, H.; Lee, T. W. Efficient visible quasi-2D perovskite light-emitting diodes. *Adv. Mater*. **2016**, *28*, 7515–7520.
[171] Yuan, M. J.; Quan, L. N.; Comin, R.; Walters, G.; Sabatini, R.; Voznyy, O.; Hoogland, S.; Zhao, Y. B.; Beauregard, E. M.; Kanjanaboos, P. et al. Perovskite energy funnels for efficient light-emitting diodes. *Nat. Nanotechnol*. **2016**, *11*, 872–877.
[172] Deschler, F.; Price, M.; Pathak, S.; Klintberg, L. E.; Jarausch, D. D.; Higler, R.; Hüttner, S.; Leijtens, T.; Stranks, S. D.; Snaith, H. J.

et al. High photoluminescence efficiency and optically pumped lasing in solution-processed mixed halide perovskite semiconductors. *J. Phys. Chem. Lett.* **2014**, *5*, 1421–1426.
[173] Zhao, J. J.; Deng, Y. H.; Wei, H. T.; Zheng, X. P.; Yu, Z. H.; Shao, Y. C.; Shield, J. E.; Huang, J. S. Strained hybrid perovskite thin films and their impact on the intrinsic stability of perovskite solar cells. *Sci. Adv.* **2017**, *3*, eaao5616.
[174] Smith, I. C.; Hoke, E. T.; Solis-Ibarra, D.; McGehee, M. D.; Karunadasa, H. I. A layered hybrid perovskite solar-cell absorber with enhanced moisture stability. *Angew. Chem., Int. Ed.* **2014**, *53*, 11232–11235.
[175] Cai, B.; Li, X. M.; Gu, Y.; Harb, M.; Li, J. H.; Xie, M. Q.; Cao, F.; Song, J. Z.; Zhang, S. L.; Cavallo, L. et al. Quantum confinement effect of two-dimensional all-inorganic halide perovskites. *Sci. China Mater.* **2017**, *60*, 811–818.
[176] Lin, Y.; Bai, Y.; Fang, Y. J.; Wang, Q.; Deng, Y. H.; Huang, J. S. Suppressed ion migration in low-dimensional perovskites. *ACS Energy Lett.* **2017**, *2*, 1571–1572.
[177] Xiao, X.; Dai, J.; Fang, Y. J.; Zhao, J. J.; Zheng, X. P.; Tang, S.; Rudd, P. N.; Zeng, X. C.; Huang, J. S. Suppressed ion migration along the in-plane direction in layered perovskites. *ACS Energy Lett.* **2018**, *3*, 684–688.
[178] Yang, X. L.; Zhang, X. W.; Deng, J. X.; Chu, Z. M.; Jiang, Q.; Meng, J. H.; Wang, P. Y.; Zhang, L. Q.; Yin, Z. G.; You, J. B. Efficient green light-emitting diodes based on quasi-two-dimensional composition and phase engineered perovskite with surface passivation. *Nat. Commun.* **2018**, *9*, 570.
[179] Xing, J.; Yan, F.; Zhao, Y. W.; Chen, S.; Yu, H. K.; Zhang, Q.; Zeng, R. G.; Demir, H. V.; Sun, X. W.; Huan, A. et al. High-efficiency light-emitting diodes of organometal halide perovskite amorphous nanoparticles. *ACS Nano* **2016**, *10*, 6623–6630.
[180] Cho, H.; Jeong, S. H.; Park, M. H.; Kim, Y. H.; Wolf, C.; Lee, C. L.; Heo, J. H.; Sadhanala, A.; Myoung, N.; Yoo, S. et al. Overcoming the electroluminescence efficiency limitations of perovskite light-emitting diodes. *Science* **2015**, *350*, 1222–1225.
[181] Tan, Z. K.; Moghaddam, R. S.; Lai, M. L.; Docampo, P.; Higler, R.; Deschler, F.; Price, M.; Sadhanala, A.; Pazos, L. M.; Credgington, D. et al. Bright light-emitting diodes based on organometal halide perovskite. *Nat. Nanotechnol.* **2014**, *9*, 687–692.
[182] Wang, J. P.; Wang, N. N.; Jin, Y. Z.; Si, J. J.; Tan, Z. K.; Du, H.; Cheng, L.; Dai, X. L.; Bai, S.; He, H. P. et al. Interfacial control toward efficient and low-voltage perovskite light-emitting diodes. *Adv. Mater.* **2015**, *27*, 2311–2316.
[183] Voznyy, O.; Sutherland, B. R.; Ip, A. H.; Zhitomirsky, D.; Sargent, E. H. Engineering charge transport by heterostructuring solution-processed semiconductors. *Nat. Rev. Mater.* **2017**, *2*, 17026.
[184] Ban, M. Y.; Zou, Y. T.; Rivett, J. P. H.; Yang, Y. G.; Thomas, T. H.; Tan, Y. S.; Song, T.; Gao, X. Y.; Credgington, D.; Deschler, F. et al. Solution-processed perovskite light emitting diodes with efficiency exceeding 15% through additive-controlled nanostructure tailoring. *Nat. Commun.* **2018**, *9*, 3892.
[185] Era, M.; Morimoto, S.; Tsutsui, T.; Saito, S. Organic-inorganic heterostructure electroluminescent device using a layered perovskite semiconductor $(C_6H_5C_2H_4NH_3)_2PbI_4$. *Appl. Phys. Lett.* **1994**, *65*, 676–678.
[186] Mitzi, D. B. Solution-processed inorganic semiconductors. *J. Mater. Chem.* **2004**, *14*, 2355–2365.
[187] Kim, Y. H.; Cho, H.; Lee, T. W. Metal halide perovskite light emitters. *Proc. Natl. Acad. Sci. USA* **2016**, *113*, 11694–11702.
[188] Li, Z. C.; Chen, Z. M.; Yang, Y. C.; Xue, Q. F.; Yip, H. L.; Cao, Y. Modulation of recombination zone position for quasi-two-dimensional blue perovskite light-emitting diodes with efficiency exceeding 5%. *Nat. Commun.* **2019**, *10*, 1027.
[189] Yu, M. T.; Yi, C.; Wang, N. N.; Zhang, L. D.; Zou, R. M.; Tong, Y. F.; Chen, H.; Cao, Y.; He, Y. R.; Wang, Y. et al. Control of barrier width in perovskite multiple quantum wells for high performance green light–emitting diodes. *Adv. Opt. Mater.* **2019**, *7*, 1801575.
[190] Zou, W.; Li, R. Z.; Zhang, S. T.; Liu, Y. L.; Wang, N. N.; Cao, Y.; Miao, Y. F.; Xu, M. M.; Guo, Q.; Di, D. W. et al. Minimising efficiency roll-off in high-brightness perovskite light-emitting diodes. *Nat. Commun.* **2018**, *9*, 608.
[191] Lin, K. B.; Xing, J.; Quan, L. N.; de Arquer, F. P. G.; Gong, X. W.; Lu, J. X.; Xie, L. Q.; Zhao, W. J.; Zhang, D.; Yan, C. Z. et al. Perovskite light-emitting diodes with external quantum efficiency exceeding 20 per cent. *Nature* **2018**, *562*, 245–248.
[192] Sun, S. Y.; Salim, T.; Mathews, N.; Duchamp, M.; Boothroyd, C.; Xing, G. C.; Sum, T. C.; Lam, Y. M. The origin of high efficiency in low-temperature solution-processable bilayer organometal halide hybrid solar cells. *Energy Environ. Sci.* **2014**, *7*, 399–407.
[193] Manser, J. S.; Kamat, P. V. Band filling with free charge carriers in organometal halide perovskites. *Nat. Photonics* **2014**, *8*, 737–743.
[194] Tanaka, K.; Takahashi, T.; Ban, T.; Kondo, T.; Uchida, K.; Miura, N. Comparative study on the excitons in lead-halide-based perovskite-type crystals $CH_3NH_3PbBr_3$ $CH_3NH_3PbI_3$. *Solid State Commun.* **2003**, *127*, 619–623.
[195] D'Innocenzo, V.; Grancini, G.; Alcocer, M. J. P.; Kandada, A. R. S.; Stranks, S. D.; Lee, M M.; Lanzani, G.; Snaith, H. J.; Petrozza, A. Excitons versus free charges in organo-lead tri-halide perovskites. *Nat. Commun.* **2014**, *5*, 3586.
[196] Kondo, S.; Takahashi, K.; Nakanish, T.; Saito, T.; Asada, H.; Nakagawa, H. High intensity photoluminescence of microcrystalline $CsPbBr_3$ films: Evidence for enhanced stimulated emission at room temperature. *Curr. Appl. Phys.* **2007**, *7*, 1–5.
[197] Tanaka, K.; Takahashi, T.; Kondo, T.; Umeda, K.; Ema, K.; Umebayashi, T.; Asai, K.; Uchida, K.; Miura, N. Electronic and excitonic structures of inorganic–organic perovskite-type quantum-well crystal $(C_4H_9NH_3)_2PbBr_4$. *Jpn. J. Appl. Phys.* **2005**, *44*, 5923–5932.
[198] Cohen, B. E.; Wierzbowska, M.; Etgar, L. High efficiency quasi 2D lead bromide perovskite solar cells using various barrier molecules. *Sustainable Energy Fuels* **2017**, *1*, 1935–1943.
[199] Li, J.; Luo, L. H.; Huang, H. W.; Ma, C.; Ye, Z. Z.; Zeng, J.; He, H. P. 2D behaviors of excitons in cesium lead halide perovskite nanoplatelets. *J. Phys. Chem. Lett.* **2017**, *8*, 1161–1168.
[200] Hu, H. W.; Salim, T.; Chen, B. B.; Lam, Y. M. Molecularly engineered organic-inorganic hybrid perovskite with multiple quantum well structure for multicolored light-emitting diodes. *Sci. Rep.* **2016**, *6*, 33546.
[201] Quan, L. N.; Zhao, Y. B, García de Arquer, F. P.; Sabatini, R.; Walters, G.; Voznyy, O.; Comin, R.; Li, Y. Y.; Fan, J. Z.; Tan, H. R. et al. Tailoring the energy landscape in quasi-2D halide perovskites enables efficient green-light emission. *Nano Lett.* **2017**, *17*, 3701–3709.
[202] Kumar, S.; Jagielski, J.; Kallikounis, N.; Kim, Y. H.; Wolf, C.; Jenny, F.; Tian, T.; Hofer, C. J.; Chiu, Y. C.; Stark, W. J. et al. Ultrapure green light-emitting diodes using two-dimensional formamidinium perovskites: Achieving recommendation 2020 color coordinates. *Nano Lett.* **2017**, *17*, 5277–5284.
[203] Zhang, W. W.; Yan, X. W.; Gao, W.; Dong, J.; Ma, R. Q.; Liu, L.; Zhang, M. The dependence of chain length of phenylalkylamine on the performance of perovskite light emitting diode. *Org. Electron.* **2019**, *65*, 56–62.